



Arab American University

Faculty of Graduate Studies

**Effect of Au nano sheets thickness on the optical dynamics
of MnO₂ nano stacked layers**

By

Azhar Imad Mahmoud Rabaya

Supervisor

Prof. Dr. Atef Fayez Qasrawi

This Thesis was submitted in partial fulfillment of the requirements for

The Master's degree in Physics

October/2021

© Arab American University-2021. All rights reserved.

Thesis Approval

Effect of Au nano sheets thickness on the optical dynamics of MnO₂ nano stacked layers

By

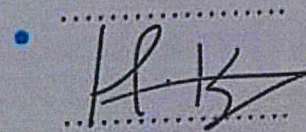
Azhar Imad Mahmud Rabaya

This thesis was defended successfully on October 2021 and approved by:

Committee members

1. Prof. Dr. Atef Fayez Qasrawi: Supervisor
2. Prof. Dr. Hazem Khanfar: Internal examiner
3. Prof. Dr. Mohammad Elsaid: External examiner

Signature

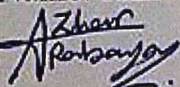


M. Elsaid

Declaration

The work in this thesis, unless otherwise referenced, is the researcher's own work and has not been submitted elsewhere for any other degree or qualification.

Student's Name: Azhar Imad Mahmoud Rabaya

Signature: 

Date: 16/1/2023

Acknowledgments

In the name of God, the Most Gracious, the Most Merciful, and my success is only by Allah. My master's thesis has been completed from my prestigious university, the Arab American University thanks to God. I extend my sincere thanks and appreciation to all faculty members. In particular, the honorable Professor Dr. Atef Qasrawi, who has spared no effort in order for the thesis to see the light. God rewarded him with the best reward ... And I also thanks to the external examiner, Prof. Dr. Mohammad saeed and the internal examiner, the Prof. Dr. Hazem Khanfar. Thank are also due to the kind assistance Rana Daraghmeah who provided me with support and assistance, both in the practical and theoretical side throughout the work. All thanks to my parents without them, I would not exist in this life, and from them I learned to be resilient, no matter the difficulties. Thanks and gratitude to my dear husband for standing with me throughout my studies. To those who have demonstrated to me what is the beautiful of life my brothers and sisters. To the taste of the most beautiful moments with my friends.

Abstract

In this thesis, manganese oxide thin films are prepared by a vacuum evaporation technique under a vacuum pressure of 10^{-5} mbar. The films are then sandwiched with Au nanosheets in the range of 5-100 nm. The structural, optical and dielectric properties of the films are studied by the X-ray diffraction and optical spectrophotometry techniques. It is observed that $\text{MnO}_2/\text{Au}/\text{MnO}_2$ nanofilms are of amorphous nature due to the possible existence of more than one polymorphic phase in its structure. Insertion of Au nanosheets between layers of MnO_2 successfully enhanced the optical reflectivity and engineered the energy band tails, energy band gap and dielectric constant as well. The achievements are presented by band gap narrowing and increasing of the dielectric constant value. It is also observed that the exponential distribution of energy band tails become wider as a result of Au/MnO_2 orbital states overlapping. In the light of the above mentioned properties MnO_2 nanosheets can be nominated for optoelectronic applications.

List of contents

Title	Page No.
List of tables	Vii
List of figures	Viii
List of Symbols	X
Chapter One Introduction	1
Chapter Two Theoretical Background	3
2.1 X-ray diffraction (XRD)	3
2.1.1 Bragg's law	4
2.1.2 Crystallography	5
2.2 Optical properties	8
2.2.1 The absorption coefficient	9
2.2.2 Tauc's equation and band gap measuring	10
2.2.3 Direct and indirect transition	11
2.2.4 Urbach Band Tails	12
2.2.5 The refractive index and the dielectric spectra	12
2.2.6 Drude-Lorentz Model	15
Chapter Three Experimental Details	18
3.1 Samples preparation	18
3.2 Ionic coating technique	19
3.3 Thin film characterization	20
3.3.1 X-ray diffraction	20
3.3.2 Optical measurements	21
3.3.3 Hot probe technique	22
Chapter Four Results and Discussion	24

4.1 Structural Analysis	24
4.2 Optical Analysis	25
4.3 Dielectric dispersion	34
Chapter Five Conclusion	37
References	38
المخلص	43

List of tables

No	Title	Page No.
2.1	The 7 lattice groups in three dimensions	6
2.2	The 14 lattice types in 3D.	7

List of figures

No	Caption	Page No.
2.1	The schematic diagram of the X-ray diffractometer.	4
2.2	The schematic diagram of Bragg scattering on the lattice surface.	5
2.3	The transmittance, reflectance and absorbance of a light incident on optical material.	8
2.4	The diagram of Snell's Law.	9
2.5	A light beam incident on an optical medium is exposed to multiple reflections.	10
2.6	Energy (E) vs crystal momentum (k) for a semiconductor with direct and indirect band gap.	11
3.1	Thermal evaporation system.	19
3.2	The optical image of the film of MnO ₂ .	19
3.3	The geometrical design of the MnO ₂ /Au/MnO ₂ films	20
3.4	The schematic of X-ray	21
3.5	The XRD technique	21
3.6	The UV-VIS spectrophotometer.	22
3.7	The hot-probe technique.	22
3.8	Hot-probe set up.	23
4.1	XRD patterns of stacked layers of MnO ₂ .	24
4.2	Transmission spectra of the MnO ₂ /Au/MnO ₂ stacked nanosheets at 300 K in the wavelength range of 190-1100 nm.	26
4.3	Reflection spectra of MnO ₂ /Au/MnO ₂ stacked nanosheets at 300K in the wavelength range of 190-1100nm.	27
4.4(a)	The variation of T spectra as function of Au nanosheet thickness	28
4.4(b)	The variation of R spectra as function of Au nanosheet thickness	28

4.5	Absorption coefficient of $\text{MnO}_2/\text{Au}/\text{MnO}_2$ stacked layers.	30
4.6	$\ln(\alpha)$ - E variation in the low absorption region for band tail investigation of the $\text{MnO}_2/\text{Au}/\text{MnO}_2$ stacked layers.	31
4.7	The energy band tails of the stacked layers of MnO_2 as function of Au nanosheet thickness.	31
4.8	Energy band gaps investigation for the $\text{MnO}_2/\text{Au}/\text{MnO}_2$ stacked layers.	33
4.9	The energy band gaps of the stacked layers of MnO_2 as function of Au nanosheet thickness.	33
4.10	Real parts of the dielectric constant of the films measured with energy.	34
4.11	(a) the values of the energy band gaps of the films measured with thickness. (b) real parts of the dielectric constant of films measured with thickness in infrared region. (c) real parts of the dielectric constant of films measured with thickness in visible region. (d) real parts of the dielectric constant of films measured with thickness in ultraviolet region.	35
4.12	Imaginary parts of the dielectric constant of the $\text{MnO}_2/\text{Au}/\text{MnO}_2$	36

List of symbols

Symbol	Symbol Meaning
Au	Gold
MnO ₂	Oxidized Manganese
E _g	Energy band gap
α	Absorption coefficient
	Transmittance
T	Reflectance
R	
θ	Bragg angle
D	Inter-planner distance
λ	Wavelength
N	Integer
D	Crystallite Size
β	The peak broadening at full width half maximum peak in radians
K	The shape factor
E ₀	The width of the band tails
$\epsilon_1(E)$	The real part of the dielectric constant
$\epsilon_2(E)$	The imaginary part of the dielectric constant
K(E)	Extinction coefficient
R(E)	The normal incidence reflectivity
ϵ_{eff}	The effective dielectric constant
μ_{eff}	The effective permeability
ϵ_s	The permittivity of semiconductor
X	The electron affinity

Chapter One

Introduction

In recent years, extensive researches have been concerned with the use of transition metal oxides, including Manganese dioxide (MnO_2). MnO_2 is a canonical compound [1]. Also, it is a robust and stable material with tunable properties which offer great surface areas [2]. Today, oxidized manganese has become important and technically attractive for applications in various fields such as catalysts, adsorption, environmental applications [3], and magnetoelectronic devices [4]. MnO_2 has also been used extensively in electrolysis and photocatalytic activities [5]. It is found that MnO_2 has four crystal phases [6], and crystallizes in many different crystalline polymorphs [7]. Such as pyrolusite (β), hollandite (α), γ types and various controlled morphologies [8]. MnO_2 can exhibit many polymorphic phases because of the combination of the basic octahedral MnO_6 units [9]. These polyphases strongly affect the crystal structure of the material and play a vital role in its optical properties [10].

Recently, MnO_2 with several phase structures are synthesized by different methods and raw materials including electrodeposition, sol-gel templating and hydrothermal methods [6]. In a previous work, the doped MnO_2 was prepared by one step hydrothermal method. The thickness of nano flakes decreased after doping, thus the transmission path of electrons in bulk material was abbreviated [8]. In addition, it has been discovered in previous research that the optical band gap energy of doped MnO_2 is narrower compared to undoped MnO_2 [11]. Also, doping of MnO_2 nanostructures leads to a red shift in the absorption edge [11]. It was discovered by the functional density theory calculations of doped MnO_2 that there is a change in the electronic properties of MnO_2 after being doped [12].

The wide range of applications of MnO_2 and the interesting features of the material that was achieved to doping, motivated us to study its structural and optical properties. Thus, here in this work, stacked layers of MnO_2 of thickness of 50 nm are sandwiched with Au nanosheets of different thicknesses. The effect of the Au nanosheets thickness on the optical transmittance, reflectance, absorption coefficient, energy band tail, energy band gap and dielectric dispersion will be explored. The

work will provide information about a method of engineering the optical properties of MnO_2 .

In the second chapter of this thesis, the necessary theoretical background that is needed for explaining the results is reported. In the third chapter, the experimental methods of preparation is reported. Particular focus on the thermal evaporation technique is given. In the fourth and fifth chapters, the obtained results are reported and discussed.

Chapter Two

Theoretical Background

2.1:X-ray diffraction (XRD)

X-ray diffraction is a common technique used to detect the nature of the materials as amorphous or crystalline. Also, it is used in many applications such as structure and phase identification, composition of solid solution, lattice constants, grain size determination, and degree of crystallinity in a mixture of crystalline and amorphous substances [13]. When the monochromatic beams of X-rays are scattered at appointed angles from each group of lattice planes in a material and a constructive interference occurs, the X-ray diffraction peaks is produced [14]. The x-ray spectra created by this technique provide a structural fingerprint of the substance. The peak height is proportional to the number of grains in a preferred orientation [15]. As shown in Fig 2.1[16], X-ray diffractometer system consisted of three basic components: a X-ray tube, a sample stage, and a X-ray detector. X-ray beams are created in a cathode ray tube by heating a filament to produce electrons. By applying avoltage,the electrons are accelerated toward a target and the target material is bombarded with electrons. When electrons have sufficient energy to eject inner shell electrons of the target material,distinctive X-ray spectra are generated. These spectra consist of many components, the generally common being K_{α} and K_{β} . For single crystal diffraction, Copper (Cu) is the most common target material with CuK_{α} radiation and energy are equal 1.5418 Å and 8.04 KeV, respectively. These X-rays are collimated and directed toward the sample. While the sample and detector is rotated, the intensity of the reflected X-rays is registered. If the incident X-rays impinging the sample fulfill Bragg's law, constructive interference happens and a peak in intensity arises. a detector registers and processes this X-ray signal and transfers the signal to account rate, which is then output to a device such as computer monitor.

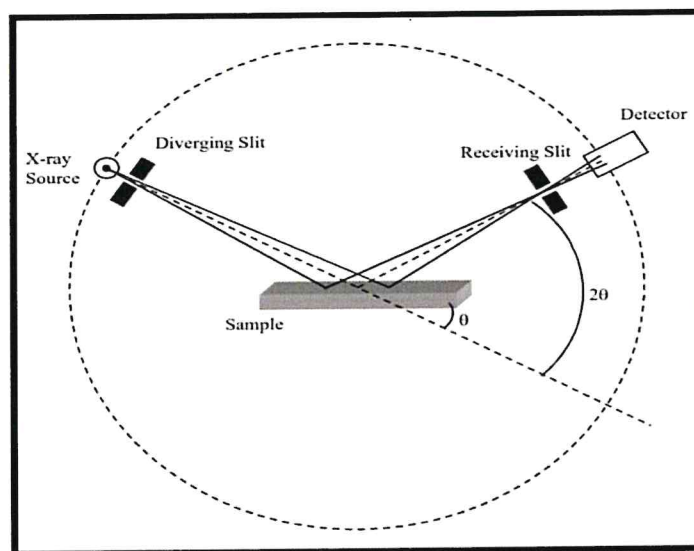


Figure 2.1: The schematic diagram of the X-ray diffractometer.

2.1.1 Bragg's Law

X-ray diffraction analysis is based on Bragg's law. The law demonstrates the relationship between an incident x-ray light and its reflection off from a crystal surface Fig 2.2 [17]. When the X-ray is incident onto a crystal surface, its angle of incidence (θ) will reflect with the same angle of scattering (θ). According to Bragg Equation, constructive interference will occur, when the path difference (d) is equal to a whole number (n) of wavelength (λ) of the reflected X-ray [17].

$$2d \sin \theta = n\lambda \quad (2.1)$$

Where, d is the interplanar distance between two plans of atoms which is measured in angstrom (\AA), θ is the angle between the incident beam and the plane surface, the integern is the order of the corresponding reflection and λ is the wavelength of the incident X-ray beam which is equaled to 1.5405 \AA .

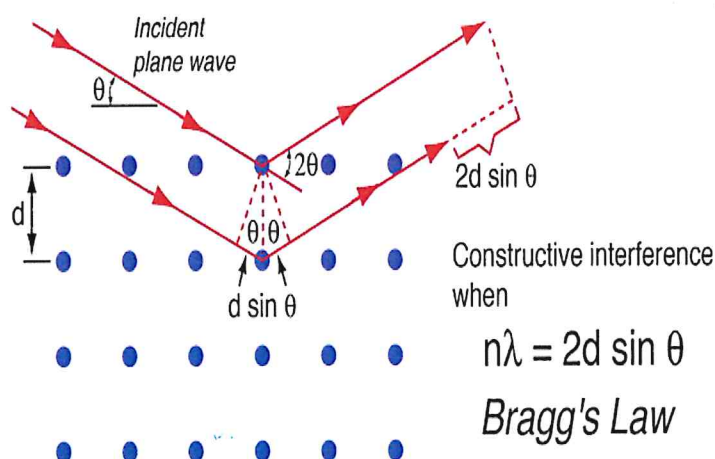


Figure 2.2: The schematic diagram of Bragg scattering on the lattice surface.

2.1.2 Crystallography

X-ray crystallography is a method for finding the arrangement of atoms within a crystal structure. A crystalline solid is created by uniform repetition of its identical building blocks (atoms or molecules) in a three dimensional periodic array. The unit cell is a basic fundamental concept in crystal structures. It is the smallest unit of volume that allows identical cells to be stacked together to fill all space. A primitive cell is a unit cell that contains only one lattice point. There are three axes that represent the dimensions of the unit cells. The lattice constants a , b and c with α , β and γ being the angles between them, also can be determined by XRD[18].

Miller indices are the mathematical representation of the crystal planes. The direction and orientation of a surface or a crystal plane may be determined by considering how the crystal plane intersects the main crystallographic axes of the solid. The enforcement of a set of principles leads to the assignment of the Miller Indices $\{hkl\}$, which are a set of numbers which quantification the intercepts and so may be used to identify the plane or surface [19].

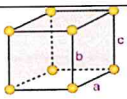
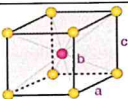
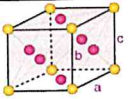
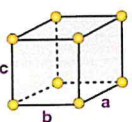
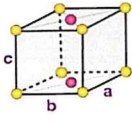
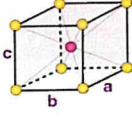
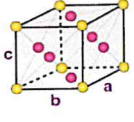
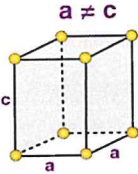
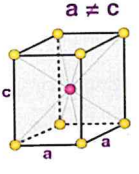
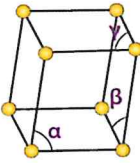
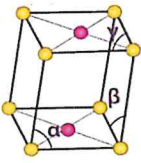
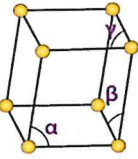
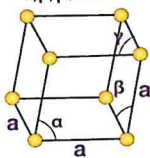
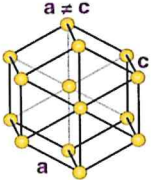
There are 14 different 3-dimensional configurations into which atoms can be arranged in crystals. These configurations are called Bravais lattices[18]. These Bravais lattices are distributed into seven systems (structures), as seen in Table 2.1 below. Also, the fourteen Bravais lattices are presented in Table 2.2. Note that the letters a_1 , a_2 , and

a_1, a_2, a_3 have been used to indicate the dimensions of the unit cells while the letters α , β , and γ indicate the corresponding angles in the unit cells.

Table 2.1 The 7 lattice groups in three dimensions

Crystal structure	Number of Bravais Lattice	Conditions
Cubic	3	$a_1 = a_2 = a_3$ $\alpha = \beta = \gamma = 90^\circ$
Hexagonal	1	$a_1 = a_2 \neq a_3$ $\alpha = \beta = 90^\circ, \gamma = 120^\circ$
Trigonal	1	$a_1 = a_2 = a_3$ $\alpha = \beta = \gamma < 120^\circ \neq 90^\circ$
Tetragonal	2	$a_1 = a_2 \neq a_3$ $\alpha = \beta = \gamma = 90^\circ$
Orthorhombic	4	$a_1 \neq a_2 \neq a_3$ $\alpha = \beta = \gamma = 90^\circ$
Monoclinic	2	$a_1 \neq a_2 \neq a_3$ $\alpha = \beta = 90^\circ \neq \gamma$
Triclinic	1	$a_1 \neq a_2 \neq a_3$ $\alpha \neq \beta \neq \gamma \neq 90^\circ$

Table 2.2 The 14 lattice types in 3D.

system	Braves lattice			
Cubic				
	Simple Cubic	Body centered cubic	Face centered cubic	
Orthorhombic				
	Simple Cubic	Base centered cubic	Body centered cubic	Face centered cubic
Tetragonal				
	Simple	Body centered		
Monoclinic				
	Centered	Simple		
Triclinic				
	Simple			
Trigonal				
	Simple			
Hexagonal				
	Simple			

2.2 Optical properties

The semiconductor materials have unique optical properties that make them important in optoelectronic applications. the study of optical properties includes the evaluation of transmittance (T), reflectance (R), absorption coefficient (α), energy gap (E_g), band tails and dispersion of dielectric constant (ϵ). Fig. 2.3 shows the transmittance, reflectance and the absorbance of incident light on optical medium.

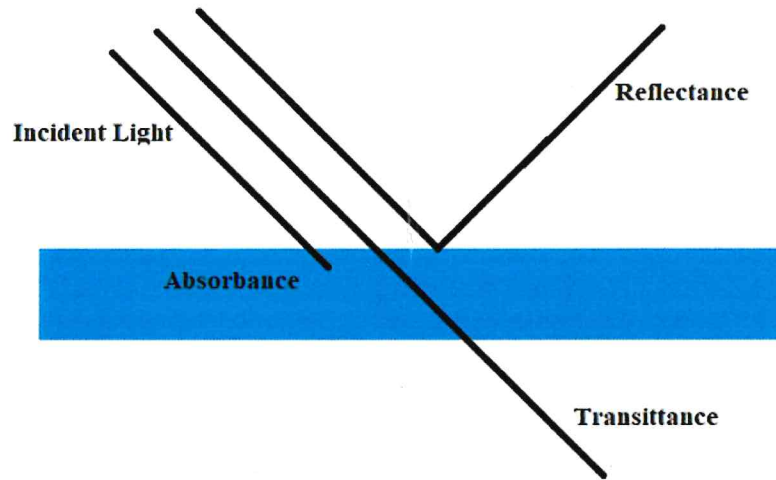


Figure 2.3: The transmittance, reflectance and absorbance of a light incident on optical material.

When light passes from one medium to another, it generally refracts, or bends. The law of refraction gives us a way of foretelling the amount of bend. The law of refraction is also known as Snell's Law. It is described the light bending at the interface between two mediums [20].

$$n_1 \sin \theta_1 = n_2 \sin \theta_2 \quad (2.2)$$

Snell's Law is displayed in the following diagram Fig 2.4. Refraction includes the angles that the incident ray and the refracted ray make with the normal to the surface at the point of refraction. The constants n are the indices of refraction for the corresponding media.

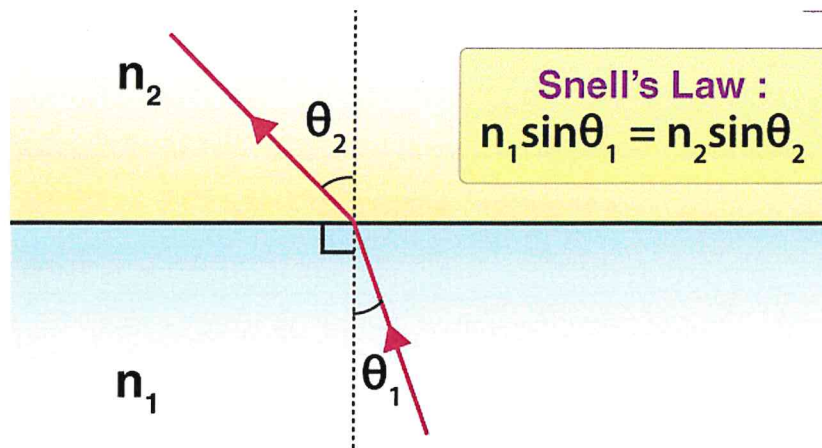


Figure 2.4: the diagram of Snell's Law.

2.2.1 The absorption coefficient

One of the most widely used techniques for obtaining information about the band structure and energy gap (E_g) of semiconductor materials is optical absorption spectrometry analysis. Absorption is strongly affected by photon-electron interaction. When light (photons) incident on an optical surface of a semiconductor material, it will be either reflected from the upper surface or absorbed into the material. Otherwise, it transmitted through the material. If an incident photon is absorbed by the optical medium, it induces an electron to exit from the valence band to conduction band. The absorption of light by an optical medium is specified by its absorption coefficient (α). Which determines to what extent into a material light of a specific wavelength can penetrate before it is absorbed. If a beam of light propagates in the z - axis, and the light intensity at point z is $I(z)$. The amount of reduction dI of the propagated light is given by:

$$dI = -\alpha I(z) dz \quad (2.3)$$

By integrating both sides of the equation (2.3) we get a formula of Beer's law [21], which state:

$$I(z) = I_0 e^{-\alpha z} \quad (2.4)$$

Where I_0 is the intensity of light at $z = 0$, α is the absorption coefficient and z is the material thickness.

The transmittance (T) of light in situation of two parallel surfaces is explained by the following expression [22, 23]:

$$T = (1 - R_1)(1 - R_2)e^{-\alpha t} \quad (2.5)$$

R_1 and R_2 represented the reflectivities of the front and back film surface, respectively. and t is the medium thickness. The term ($e^{-\alpha t}$) is the exponential decreased in the light intensity according to Beer's law.

In the situation of two materials deposited on the glass substrate, the term ($1 - R_3$) should be added in the equation (2.5).

The transmittance (T) of the multi-layer film can be written as,

$$T = \frac{(1 - R_1)(1 - R_2)(1 - R_3)e^{-\alpha t}}{1 - R_1R_2R_3e^{(-2\alpha t - 3Rt)}} \quad (2.6)$$

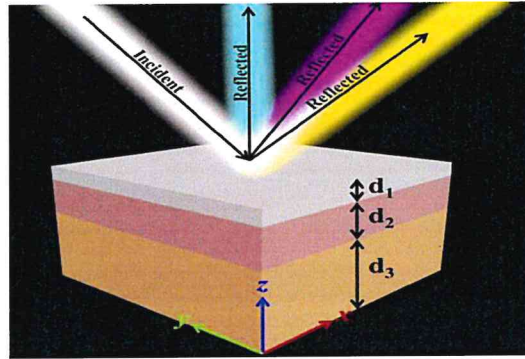


Figure 2.5 : a light beam incident on an optical medium is exposed to multiple reflections.

In our study, for three materials deposited on a glass substrate the absorption coefficient is given by:

$$\alpha = -\frac{1}{t} \ln \left(\frac{T}{(1 - R_1)(1 - R_2)(1 - R_3)(1 - R_4)} \right) \quad (2.7)$$

In this work R_1 , R_2 , R_3 and R_4 are the reflectance of glass, MnO_2 , MnO_2/Au and $\text{MnO}_2/\text{Au}/\text{MnO}_2$, respectively.

2.2.2 Tauc's equation

Tauc's equation with the help of spectra of the absorption coefficient is used to find the optical band gap for semiconductor materials. This equation shows that the energy band gap (E_g) of the materials is directly proportional to $(\alpha E)^p$ as given in the following equation [24], in which the exponent (p) indicates the nature of the transition.

$$(\alpha E)^{1/p} = B (E - E_g) \quad (2.8)$$

Where B is a constant that is fundamentally depending on the transition probability of an electron, p is an index that indicates the type of the optical absorption process and it is theoretically equal the values 2, $1/2$, 3, and $3/2$ for indirect allowed, direct allowed, indirect forbidden and direct forbidden electronic transition, respectively, E is the incident photon energy, E_g is the energy band gap.

The energy gap (E_g) is determined by plotting a graph of $(\alpha E)^{\frac{1}{p}}$ versus photon energy. Then take it in the high absorption region upon linear fitting the widest range of linear data. The value of E_g will be determined by the intercept on the photon energy (E) axes.

2.2.3 Direct and indirect transition

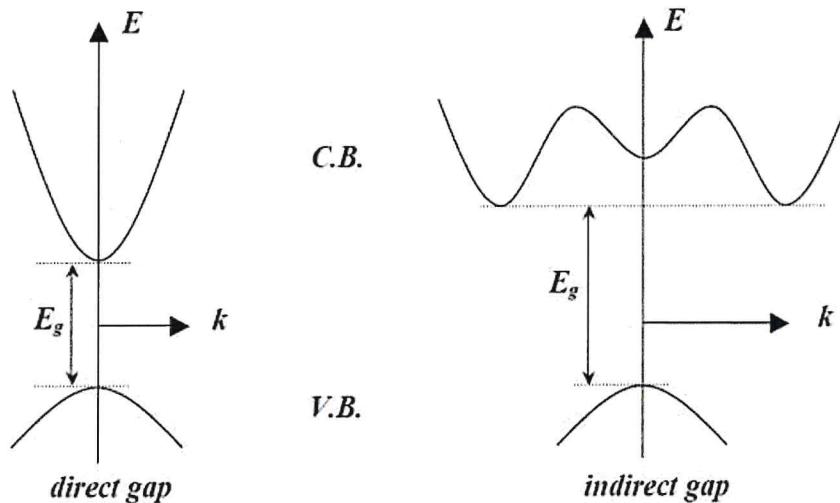


Figure 2.6: Energy (E) vs crystal momentum (k) for a semiconductor with direct and indirect band gap.

In semiconductor physics, the band gap is permanently one of two types, a direct band gap or an indirect band gap. The lowest energy states in the conduction band (CB) and the highest energy state in the valence band (VB) is recognized by a certain k -vector in the Brillouin zone. If k -vectors are similar, it is called direct band gaps. If they are dissimilar it is called an indirect band gap [25]. In direct band gaps the electrons can shift from the conduction band to the valence band without any change in crystal momentum (k -vectors) as shown in Fig 2.6. While in indirect band gaps the electron cannot shift from the minimum energy state in the conduction band to the maximum energy state in the valence band without a change in the K -vectors. The difference in the crystal momentum (k -vectors) displays biased bands that require a phonon

assistance for excited electrons to be absorbed into the conduction band. While, for the direct band gap materials, a change in the k - vectors isn't involved and no phonon assistance is needed. As shown in Fig 2.6, almost all of the energy comes from the photon (direct band), while almost all of the momentum comes from a phonon (indirect band) [25].

2.2.4 Urbach Band Tails

The absorption coefficient equips enormous physical information. From the α - E curve, if α displays constant trends of variation with changing the photon energy (E), this called the absorption saturation. In the low energy region, if α displays decreasing trends of variation with decreasing the photon energy (E), this indicates the presence of band tails. When α displays increasing trends of variation as the photon energy (E) decreases, this indicates the existence of free carrier absorption. While the interband is created when α remains constant with decreases the photon energy [26, 27]. Along the absorption coefficient curve and near the optical band edge there is an exponential part called band tail dependence on the photon energy (E) for many materials [24]. The band tails is often appeared in amorphous semiconductors, that is due to amorphous semiconductors have more disorder than the crystalline counterparts, and also these band tails are localized electronic states that are extended in the band gap [24]. The Urbach band rule is given by the following equation:

$$\alpha = \alpha_o e^{E/E_e} \quad (2.9)$$

Where α is the absorption coefficient, α_o is a constant, E is the photon energy and E_e is the energy of the band tail called Urbach energy. By taking the logarithm of the two sides of the equation (2.9), we can get a straight line equation. It is given by:

$$\ln \alpha = \ln \alpha_o + \left(\frac{E}{E_e} \right) \quad (2.10)$$

The energy band tail can be determined from the slope of the straight line of plotting $\ln(\alpha)$ as a function of incident photon energy (E).

2.2.5 The refractive index and the dielectric spectra

Dielectric spectra are very important as they are the main source of electromagnetic energy storage. In optics, the refractive index also known as indices of refraction of a material is a dimensionless number that demonstrates how fast light passes through the material. It is a complex number consists of imaginary and real parts and depends

on the incident optical beam's wavelength [28]. The material efficiency of field energy storage was explained by the real part of the permittivity. While the imaginary part handles the losses of energy due to the variation of applied field.

The complex dielectric function can be determined through introducing Maxwell's equations [29].

$$\nabla \times H - \frac{1}{c} \frac{\partial D}{\partial t} = \frac{4\pi}{c} j \quad (2.11)$$

$$\nabla \times E + \frac{1}{c} \frac{\partial B}{\partial t} = 0 \quad (2.12) \quad \nabla \cdot D = 0$$

$$(2.13)$$

$$\nabla \cdot B = 0 \quad (2.14) \quad \text{Where:}$$

$$D = \varepsilon E \quad (2.15)$$

$$B = \mu H \quad (2.16) \quad j = \sigma E \quad (2.17)$$

the wave equation for the field E is:

$$\nabla^2 E = \frac{\varepsilon \mu}{c^2} \frac{\partial^2 E}{\partial t^2} + \frac{4\pi \sigma \mu}{c^2} \frac{\partial E}{\partial t} \quad (2.18)$$

For optical fields the sinusoidal solution is considered as the plane wave equation[30]:

$$E = E_0 e^{i(K \cdot r - \omega t)} \quad (2.19)$$

Where K is a complex propagation constant and ω is the frequency of the light. To obtain the dispersion relation substituting an equation (2.19) in (2.18):

$$-K^2 = -\frac{\varepsilon \mu \omega^2}{c^2} - \frac{4\pi i \sigma \mu \omega}{c^2} \quad (2.20)$$

In general, the dielectric constant ε and the wave vector k are complex quantities [31].

$$\varepsilon(E) = \varepsilon_r(E) + i\varepsilon_{im}(E) \quad (2.21)$$

The complex refractive index $n^*(E)$ can be determined as follows:

$$n^*(E) = n(E) + ik(E) \quad (2.22)$$

Where $n(E)$ is the real refractive index and $k(E)$ is the extinction coefficient.

$$n^*(E) = [\varepsilon(E)]^{1/2} = [\varepsilon_r(E) + i\varepsilon_{im}(E)]^{1/2} \quad (2.23)$$

From equation (2.23), it follows that

$$\varepsilon_r(E) = n(E)^2 - k(E)^2 \quad (2.24a) \quad \varepsilon_{im}(E) = 2n(E)k(E) \quad (2.24b)$$

And

$$n(E) = \left\{ \frac{[\varepsilon_r(E)^2 + \varepsilon_{im}(E)^2]^{1/2} + \varepsilon_r(E)}{2} \right\}^{1/2} \quad (2.25)$$

$$k(E) = \left\{ \frac{[\varepsilon_r(E)^2 + \varepsilon_{im}(E)^2]^{1/2} - \varepsilon_r(E)}{2} \right\}^{1/2} \quad (2.26)$$

Then the normal-incidence reflectivity $R(E)$ can be written as:

$$R(E) = \left(\frac{n(E)-1}{n(E)+1} \right)^2 \quad (2.27)$$

Substituting an equation (2.22) in $R(E)$ gives us:

$$R(E) = \frac{n(E)^2 - 2n(E) + 1 + k(E)^2}{n(E)^2 + 2n(E) + 1 + k(E)^2} = \frac{(n(E)-1)^2 + k(E)^2}{(n(E)+1)^2 + k(E)^2} \quad (2.28)$$

Since $n(E) = \sqrt{\varepsilon_{eff}\mu_{eff}}$ where ε_{eff} and μ_{eff} are the effective permittivity and permeability of a material. For nonmagnetic material the effective permeability ($\mu_{eff} = 1$).

Therefore, $n(E) = \sqrt{\varepsilon_{eff}}$, substituting in an equation (2.28) gives us:

$$R(E) = \frac{(\sqrt{\varepsilon_{eff}}-1)^2 + k(E)^2}{(\sqrt{\varepsilon_{eff}}+1)^2 + k(E)^2} \quad (2.29)$$

Where $\varepsilon_{eff} = \varepsilon_r - i\varepsilon_{im}$, ε_r and ε_{im} are the real and imaginary dielectric constant which can be written as

$$\varepsilon_r = \varepsilon_{eff} - k(E)^2 \quad (2.30a)$$

$$\varepsilon_{im} = 2\sqrt{\varepsilon_{eff}}k(E) \quad (2.30b)$$

The extinction coefficient plays an important role in determining many optical measurements. In particular, it attaches the absorption of light waves in the medium to the dielectric constant. The extinction coefficient (k) is a function of the incident photon energy (E) for the samples measures the fraction of light lost because of the absorption and scattering per unit distance of the penetration medium [31].

$$k(E) = \frac{\alpha(E)}{4\pi} \lambda \quad (2.31)$$

Where λ is the wavelength of light .

$\epsilon_r, \epsilon_{im}, k$ are all frequency dependent.

2.2.6 Drude-Lorentz Model

Dipole oscillations produced when the electric field (E) of the electromagnetic waves reacts with the dielectric materials. According to Drude-Lorentz model, electrons heading to the positively charged nucleus vibrate about an equilibrium position with a specific resonant frequency. By considering the oscillations of a free electron caused by AC electric fields of a light wave polarized over the x-axis. thus, The equation of motion that describes the electron motion is given by the following:

$$m_o \frac{d^2x}{dt^2} + m_o \gamma \frac{dx}{dt} + m_o \omega_o^2 x = -e E \quad (2.32)$$

Where m_o is the mass of the electron, x is the electron displacement, γ is the damping coefficient, ω_o is the resonant frequency, e is the charge of the electron and E is the electric field. The right side of the equation contain the driving force term. Where the left side contain accelerating, damping and restored force terms. When a time dependent incident lights electric field with a frequency ω interacts with electrons, the electric field is then expressed by the following equation:

$$E(t) = E_o \cos(\omega t + \phi) = E_o \text{Re}(\exp(-i\omega t - \phi)) \quad (2.33)$$

Where E_o is the electric field amplitude and ϕ is the light phase. The AC electric field brings on oscillations can be expressed as:

$$X(t) = X_o \text{Re}(\exp(-i\omega t - \phi')) \quad (2.34)$$

Where X_o and ϕ' is the amplitude of the electron displacement and the phase of oscillation, respectively. X_o and E_o must be complex numbers. Then, we find the first and second derivative of the electron displacement with respect to time as follow :

$$\frac{dx}{dt} = X_o (-i\omega) e^{-i\omega t} \quad (2.35)$$

$$\frac{d^2x}{dt^2} = X_o (-i\omega)^2 e^{-i\omega t} = -X_o \omega^2 e^{-i\omega t} \quad (2.36)$$

By substituting the equations (2.33), (2.34), (2.35) and (2.36) in the equation of motion (2.32) we get:

$$-m_o \omega^2 X_o e^{-i\omega t} - m_o \gamma \omega X_o e^{-i\omega t} + m_o \omega_o^2 X_o e^{-i\omega t} = -e E_o e^{-i\omega t} \quad (2.37)$$

Dividing the equation (2.37) by $m_0 e^{-i\omega t}$, then rearranging it we get:

$$X_o = -\frac{\frac{e}{m_0} E_o}{(\omega_o^2 - \omega^2 - i\gamma\omega)} \quad (2.38)$$

A time dependent dipole moment $p(t)$ results from the frequency variant, participates in the resonant polarization induction. The dipole moment per unit volume is defined as Polarization and it can be expressed as follow:

$$p_{resonant} = Np$$

$$= -Nex \quad (2.39)$$

Substituting the equation (2.38) in the equation (2.39), gives:

$$p_{resonant} = \frac{Ne^2}{m_0} \frac{1}{\omega_o^2 - \omega^2 - i\gamma\omega} E \quad (2.40)$$

N is the number of atoms per unit volume. when the incident light frequency is equals the material natural frequency ω_o , we get the maximum polarization. The electrical displacement D of solids depends on the polarization and the electric displacement as follows:

$$D = \epsilon_o E + P \quad (2.41)$$

Otherwise, the oscillation is ignored if $\omega \neq \omega_o$, the polarization can be classed into a resonant and nonresonant parts.

$$D = \epsilon_o E + p_{background} + p_{resonant}$$

$$= \epsilon_o E + \epsilon_o \chi E + p_{resonant} \quad (2.42)$$

Here χ is the electric susceptibility.

Assuming the material is isotropic, possessing the same characteristics in all directions, and having no preferred axis. The electric displacement can be defined as:

$$D = \epsilon_o \epsilon_r E \quad (2.43)$$

ϵ_r is the relative dielectric constant. Substituting the equation (2.42) in (2.43) and using the resonant polarization definition in Equ. (2.40), the relative dielectric constant can be expressed as the following:

$$\epsilon_r(\omega) = 1 + \chi + \frac{Ne^2}{\epsilon_o m_0} \left(\frac{1}{\omega_o^2 - \omega^2 - i\gamma\omega} \right) \quad (2.44)$$

The equation (2.44) was separated into the real (ε_1) and imaginary (ε_2) parts as follows:

$$\varepsilon_1(\omega) = 1 + \chi + \frac{Ne^2}{\varepsilon_0 m_o} \left(\frac{\omega_o - \omega^2}{(\omega_o^2 - \omega^2)^2 + (\gamma\omega)^2} \right) \quad (2.45)$$

$$\varepsilon_2(\omega) = \frac{Ne^2}{\varepsilon_0 m_o} \left(\frac{\gamma\omega}{(\omega_o^2 - \omega^2)^2 + (\gamma\omega)^2} \right) \quad (2.46)$$

Chapter Three

Experimental details

In this chapter, we report the experimental details, procedures, techniques and devices used for measurements. Namely, the thermal vapor deposition technique, the X-ray diffraction technique (XRD) and the UV-VIS-NIR spectroscopy technique is explained in this chapter.

3.1 Samples preparation

The glass slides were cleaned by washing these with a softening sponge, detergent, distilled water and alcohol. Then, the cleaned glass slides were immersed in a beaker filled with alcohol. The beaker was put on the heater and heated for 15 minutes, to rift proteins that are expected to be attached onto the glass substrates. Thereafter, they were ultrasonically cleaned at 60°C for 20 minutes. Then, they were washed with alcohol and dried. We used the cleaned substrates to deposit a 50nm thin film from manganese oxide powders by using the thermal vapor deposition system which is shown in Fig.3.1. During the deposition cycle we applied the following steps. At the beginning , the glass slides were located onto the substrate holder. Then, the shutter, the vent and the chamber were closed sequentially. After that, the main power key was turn on and the operation of roughing pump followed. When the vacuum pressure reached 10 mbar, the turbo pump was turn on. Then, we waited until the pressure reaches 10^{-5} mbar. There after we opened an INFICON STM-2 thickness monitor. Then the links between the system which are responsible of thickness monitoring and software are checked. The current is increased at a slow rate to start evaporation cycle. When the compound melts, the shutter was opened and the evaporation rate was kept constant. After the targeted thickness is reached, the shutter is closed and the current is turned off, the system is kept on until is cooled. Finally, we waited until the pressure reaches 400 mbar, and then open the system. The optical image and the geometrical design of the prepared films are shown in Fig. 3.2 (a) and (b).

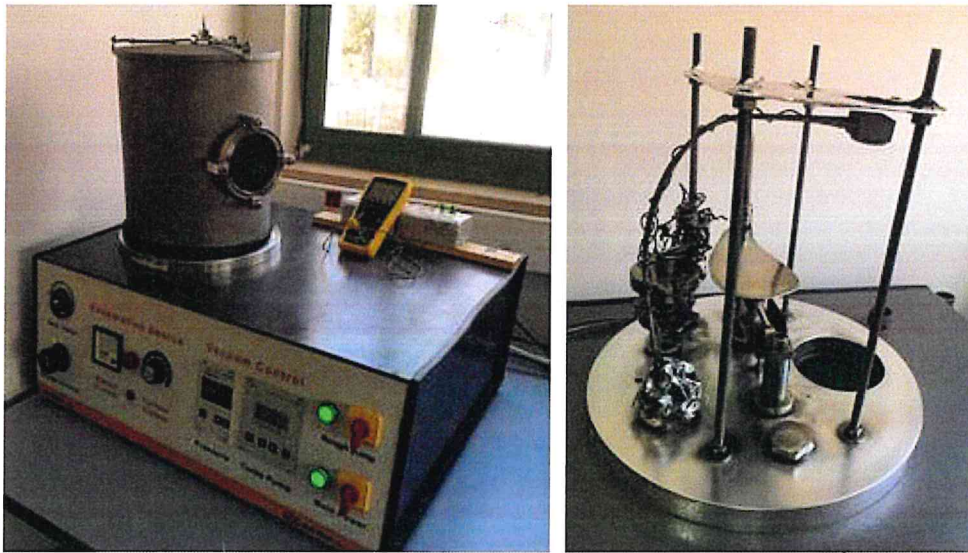


Figure3.1: Thermal evaporation system

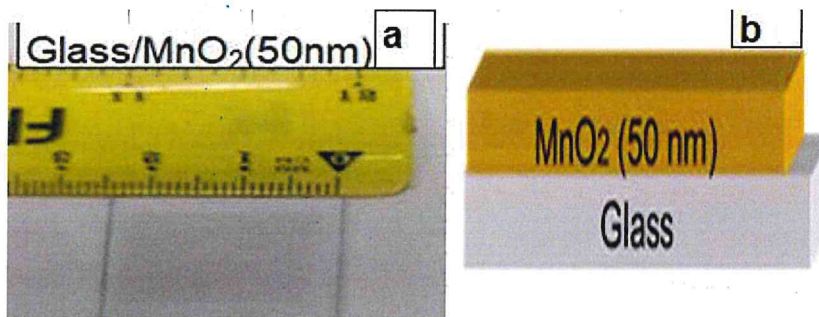


Figure3.2: (a) the optical image of the film of MnO_2 and (b) the geometrical design of the MnO_2 film.

3.2 Ionic coating technique

The ion coater is a device based on the principle of deposition gold ions onto the films. Ionic coating technique was used to coat gold sheets (Au) of different thickness onto 50nm of MnO_2 film. The geometrical design for the prepared films (MnO_2/Au) is shown in Fig 3.3. After that, 50nm of MnO_2 was evaporated onto MnO_2/Au samples, by using the thermal vapor deposition system which was explained in section 3.1. The geometrical design for the prepared film are shown in Fig. 3.3.

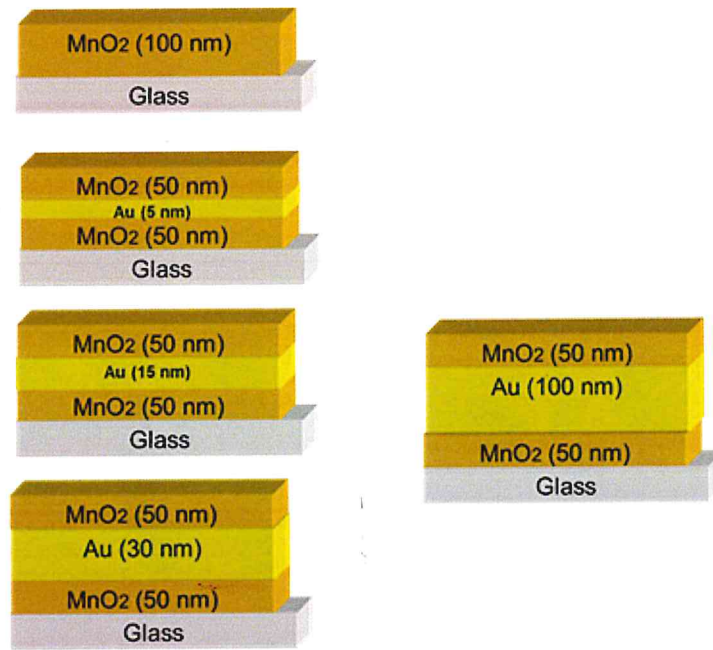


Figure (3.3): the geometrical design of the $\text{MnO}_2/\text{Au}/\text{MnO}_2$ films

3.3 Thin film characterization

3.3.1 X-ray diffraction

The X-ray diffraction analysis is used to explore the structure of materials. Bragg equation is employed to describe the diffraction process by finding the Miller indices of the crystal planes, crystal structure and the lattice constant [32]. By applying Bragg's law, a constructive interference will happen when the path difference is an integral (n) multiple of the incident wavelength (λ) [33]. The MnO_2 film is structurally characterized by Rigaku diffractometer with copper anode (Cu) $K\alpha$ radiation operating at 40kV and 15mA. In a 2θ range of $10^\circ - 70^\circ$. XRD patterns were recorded at a scanning rate of $1^\circ/\text{min}$ and the step size of 0.05° . The system is composed of a detector, a sample holder, a monochromator and a slit set. the detector collects the intensity of the X-ray beam. The size and shape of the X-ray beam is also controlled by using the slits. A software package connected to the system is used to collect the data. The X-ray diffractometer recorded the intensity as a function of 2θ . The schematic of X-ray diffraction is shown in Fig (3.4). The Rigaku MiniFlex 600 X-ray diffractometer is shown in Fig 3.5.

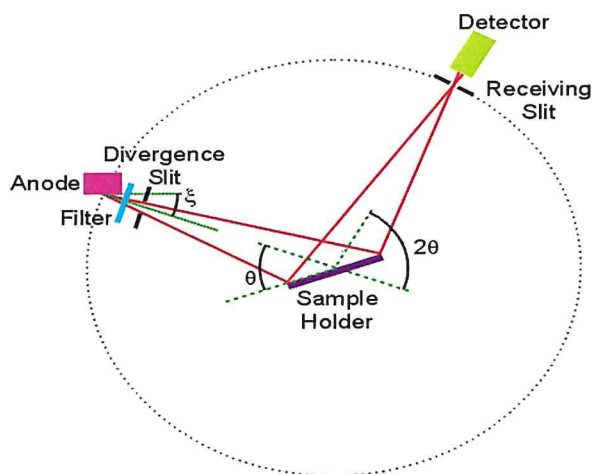
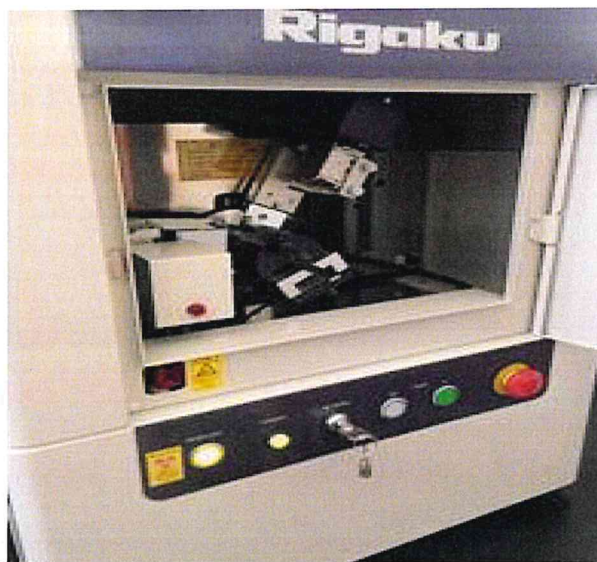


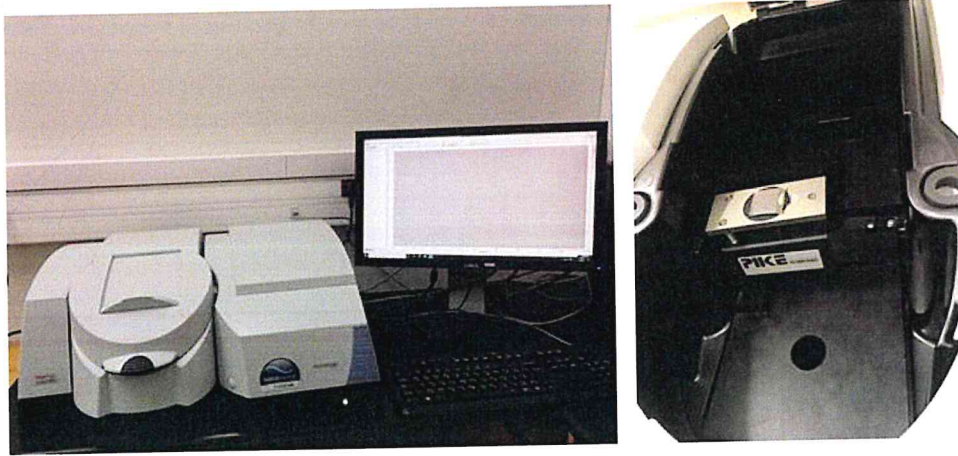
Figure3.4: The schematic of x-ray diffractometer



Figure(3.5): the XRD technique

3.3.2 Optical Measurements

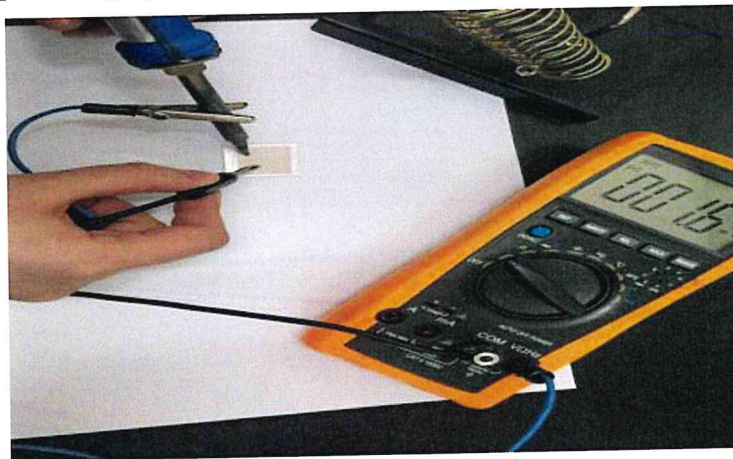
The optical properties offered by transmittance and reflectance spectra were measured in the spectral wavelength range of 300–1100 nm at a scanning speed of 1200 nm/min using a thermoscientific Evolution 300 ultraviolet–visible light (UV-VIS) spectrophotometer which is shown in Fig (3.6). The T% and R% are used to find the absorption coefficient (α), interband transition, optical energy band gaps (E_g), band tails (E_o) and dielectric dispersion (ϵ). The Vision Pro software package was used to collect and analyze the optical spectroscopic data.



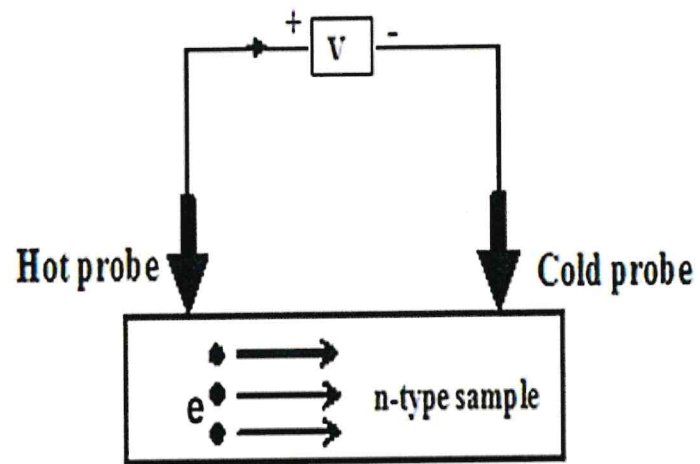
Figure(3.6):the UV-VIS spectrophotometer.

3.3.3 Hot probe technique

The Hot probe technique is a method to know the conductivity type of the semiconductors. The technique contacting a sample wafer with a "hot probe" for example, a heat soldering iron and a "cold probe", as shown in Fig (3.7). The digital multi-meter (DMM) is used to attach the cold probe and hot probe with the semiconductor surface. The hot probe was connected to the positive terminal of the (DMM) while the cold probe were connected to the negative terminal. If the (DMM) obtain a positive voltage reading, the material is n-type, while if it reads a negative voltage, the semiconductor is p-type. The negative voltage for a p-type semiconductor is generated because of holes are exited and diffused out from the hot end to the cold end. On the other hand, the positive voltage is generated for n-type due to the electrons diffusion out by concentration gradient [34]. The setup of the hot probe technique is displayed in Fig 3.8.



Figure(3.7): the hot probe technique.



Figure(3.8): hot probe set up.

Chapter four

Results and discussions

4.1 Structural analysis

The results that arise from the X-ray diffraction measurements on stacked layers of MnO_2 of thickness of 50nm are coated onto glass substrates and sandwiched with Au layers of different thickness in the range of 5-100 nm are discussed in this section. Fig. 4.1 shows the X-ray diffraction patterns for the $\text{MnO}_2/\text{Au}/\text{MnO}_2$ stacked nanosheets. The figure did not show any intensive peak for all stacked layers of MnO_2 , which means that the manganese oxide is amorphous in nature regardless of the Au nanosheet thickness.

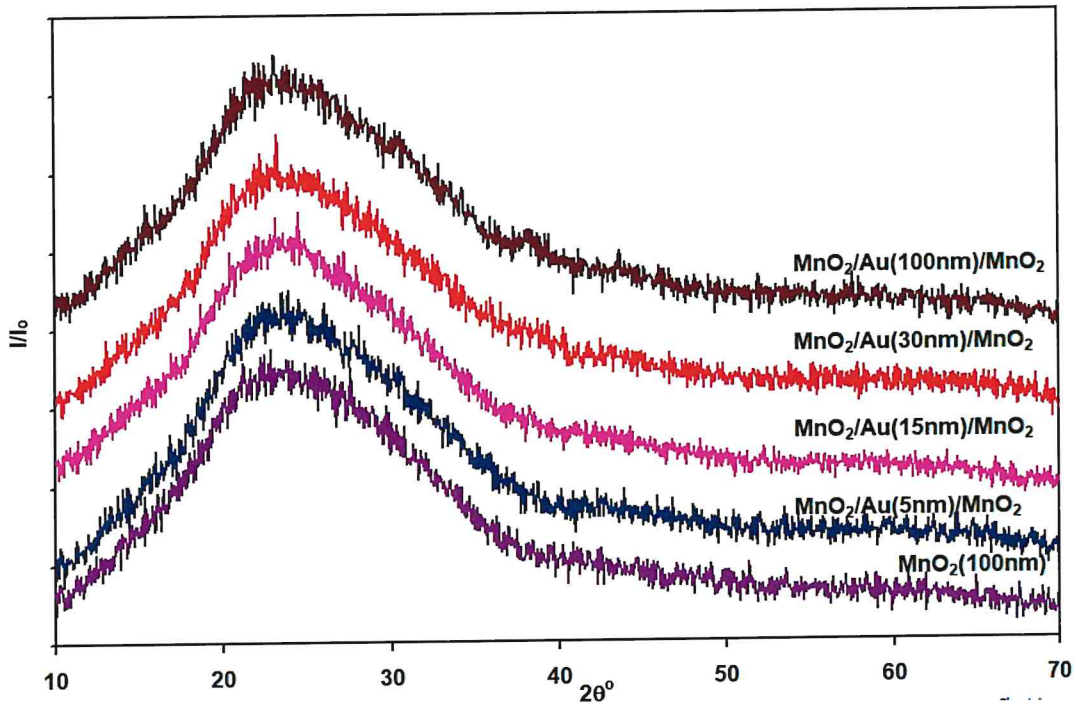


Figure (4.1): XRD patterns of stacked layers of MnO_2 .

Previous investigations into MnO_2 have reported that MnO_2 has many crystal phases [6], Such as, cubic, monoclinic, tetragonal and hexagonal structures [35]. The presence of these phases at a time in the film causes polymorphic structure and because of the large random orientations of the various types of the structures, the amorphous phase becomes favorite. MnO_2 can exhibit α and β polymorphic phases. Which α – phase (JCPDSNO. 044-0141) is best oriented along (211) plane

orientation β phase (JCPDSNO: 024-0735) is best oriented along (101) direction. The major difference between the two planes make the XRD reflection less intensive, hence the overall structures are amorphous. JCPDS: Joint Committee Powder Diffraction Standards.

4.2 Optical analysis

In order to study the effect of the Au nanosheets thickness on the optical properties of MnO_2 nano stacked layers, the transmittance (T%), reflectance (R%) and the absorption coefficient spectra of $\text{MnO}_2/\text{Au}/\text{MnO}_2$ stacked nanosheets are recorded in the wavelength (λ) range of 190-1100 nm. The thickness of MnO_2 stacked layers plays a crucial role in the optical properties. The data are presented in Fig 4.2, Fig 4.3 and Fig 4.5 respectively. As specified in Fig 4.2, the transmittance is similar for all samples in the range of 300-350nm. As the incident light wavelength of the exceeds 350nm, T spectra show decreasing trend of variations. The $\text{MnO}_2(100\text{nm})$ films is highly transparent in all range of light spectra. For the other samples, in the range of 350-920 nm, the transparency decreases with increasing Au layer thicknesses. It is also readable that for the $\text{MnO}_2(100\text{nm})$ and $\text{MnO}_2/\text{Au}(5\text{nm})/\text{MnO}_2$ samples, the transmittance increased with increasing incident light wavelengths in the range of 350-500nm, then, it remains constant in all the studied range. For $\text{MnO}_2/\text{Au}(15\text{nm})/\text{MnO}_2$ sample, the transmittance increased with increasing incident wavelengths in the range of 350-520nm, and reached the highest value at 520nm. In the range of 520-760nm it slightly decreased with increasing incident light wavelengths. Then, T% remains constant. For $\text{MnO}_2/\text{Au}(30\text{nm})/\text{MnO}_2$ and $\text{MnO}_2/\text{Au}(100\text{nm})/\text{MnO}_2$ samples, the transmittance increased with increasing incident wavelengths in the range of 350-550nm, and reached the highest value at 550nm. After that T% decreased dramatically. We noticed that, as the gold layer thickness increased from 5 to 100nm, the transmittance spectra exhibit lower values and

redshift.

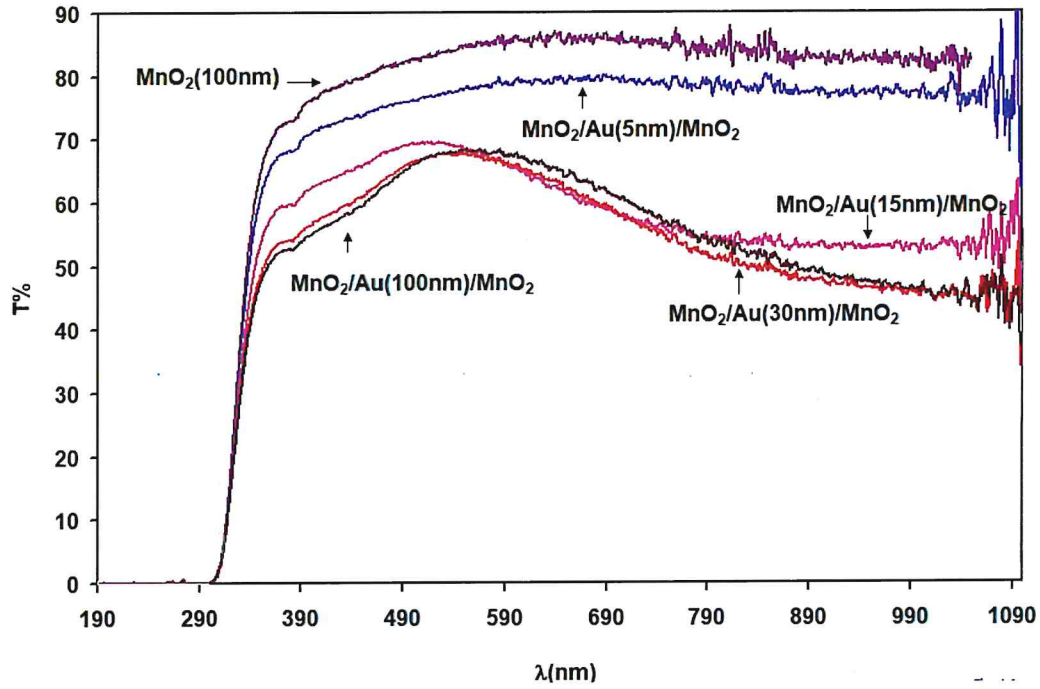


Figure 4.2: Transmission spectra of MnO₂/Au/MnO₂ stacked nanosheets at 300K in the wavelength range of 190-1100 nm.

Similarly, the measured reflectance spectra are shown in Fig 4.3. The figure shows an increase in reflectance values with increasing Au layer thickness. For samples of Au thicknesses of 15, 30 and 100 nm, R% spectra show three regions. In the range of 190-360 nm reflectance increased with increasing incident light wavelengths. In the range of 360-500 nm, it decreased with increasing incident wavelengths. After the wavelength reached 500, the R% values are increased again.

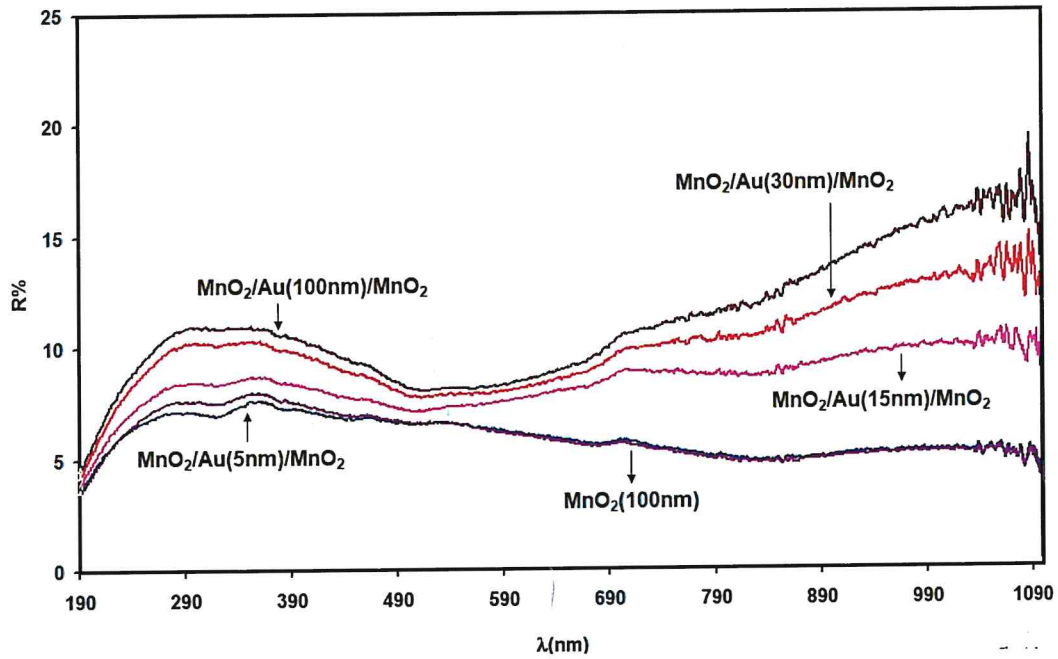


Figure 4.3: Reflection spectra of $\text{MnO}_2/\text{Au}/\text{MnO}_2$ stacked nanosheets at 300K in the wavelength range of 190-1100nm.

The variation of T and R spectra as function of Au nanosheet thickness is displayed in Fig 4.4 (a) and (b), respectively. Three regions are selected to represent the T, R- t (nm) variations. Namely, in the ultraviolet region of light, while T is decreasing, R is increasing. In the visible range of light, T spectra show decreasing trend of variations, while R spectra show increasing trend of variations. In addition, the IR range of light, the transmittance decreased with increasing Au nanosheet thickness, while the reflectance increased with increasing Au nanosheet thickness.

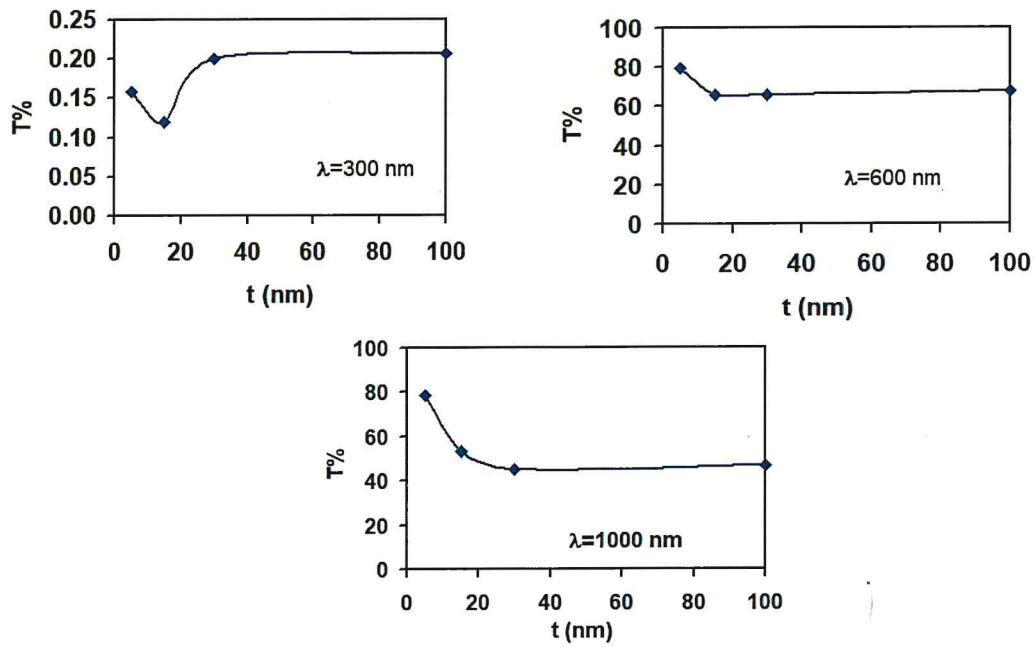


Figure 4.4 (a): The variation of T spectra as function of Au nanosheet thickness.

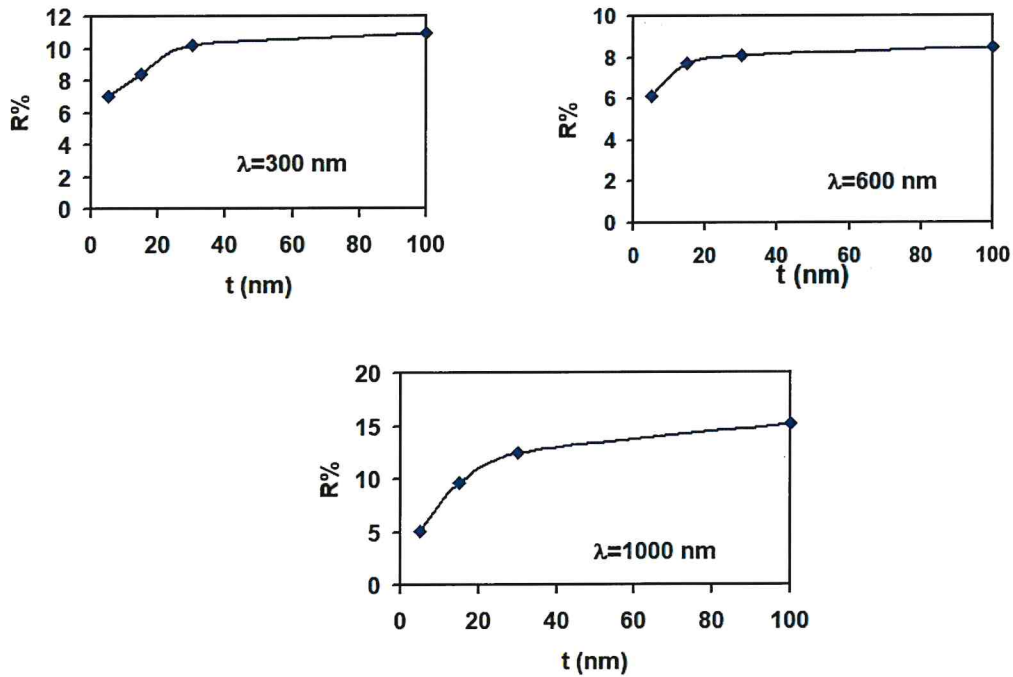


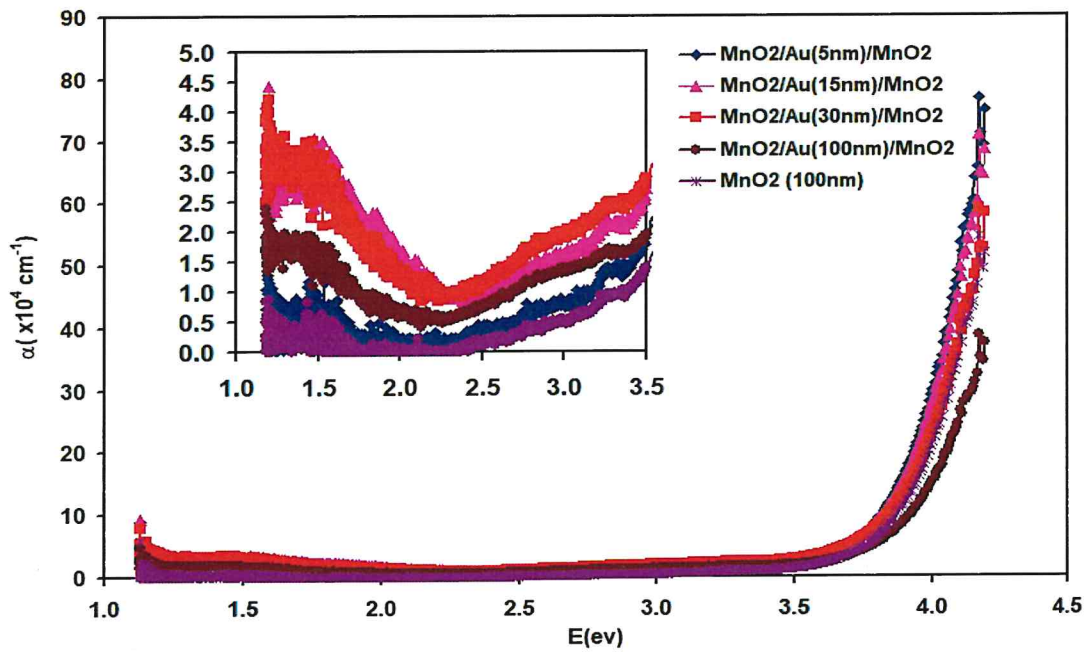
Figure 4.4 (b): The variation of R spectra as function of Au nanosheet thickness.

On the other hand, analysis of optical absorption spectra is one of the most productive material for developing and understanding the energy gap and band structure of both

amorphous and crystalline non-metallic materials. The absorption coefficient values (α) are determined using equation (4.1).

$$\alpha = -\frac{1}{t} \ln \left(\frac{T}{(1-R_1)(1-R_2)(1-R_3)(1-R_4)} \right) \quad (4.1)$$

Where t is film thickness, the calculated α values of $\text{MnO}_2/\text{Au}/\text{MnO}_2$ stacked layers with different thicknesses of Au layers as a function of incident Energy (E) is depicted in Fig (4.5). It can be seen that all samples exhibit the same trend of variation. Particularly, the absorption coefficient increases with increasing incident photon energy. Also, we note that in the spectral range of 3.8-4.2 eV, the absorption coefficient is high and decaying trend is sharp. As we show in the inset of the figure, the absorption coefficient decreases with decreasing energy in the spectral range of 2.5-3.5 eV. Such behavior is assigned to the presence of some extended band tails in the energy band gap [36]. Band tails are defined as the width of the localized states obtainable in the optical band gap that effects on the optical transitions and optical band gap structure [36]. The band tails in the semiconductor are additionally formed by inhomogeneities, impurities, vacancy and broken bonds [37]. Moreover, the presence of huge number of defects and the orbital overlapping between energy levels which is associated with amorphous structures is an other reason for band tails [38]. In the spectral range of 1.18-2.0 eV, the absorption coefficient increases with the decreasing incident energy. This behavior could be due to the high free carrier absorption. The free carrier absorption arises from the presence of free electrons and holes [39]. Also, The free carrier absorption occurs as result of the carrier transitions within conduction and valence bands [40] and lattice distortions [41].



Figure(4.5): Absorption coefficient of $\text{MnO}_2/\text{Au}/\text{MnO}_2$ stacked layer..

To determine the effect of Au layers on the width of the band tails (E_e) that is predictable to exhibit exponential bands distribution in the energy band gap of MnO_2 , $\ln(\alpha) - E$ dependence in accordance with the equation $\alpha \propto \exp(E/E_e)$ was used [40]. The E_e can be determined from the reciprocal of the linear slope of $\ln(\alpha) - E$ variations. The linear plots shown in Figure (4.6) reveal E_e values of 0.36, 0.43, 0.99, 1.07, 1.07 eV for $\text{MnO}_2/\text{Au}(0\text{nm})/\text{MnO}_2$, $\text{MnO}_2/\text{Au}(5\text{nm})/\text{MnO}_2$, $\text{MnO}_2/\text{Au}(15\text{nm})/\text{MnO}_2$, $\text{MnO}_2/\text{Au}(30\text{nm})/\text{MnO}_2$ and $\text{MnO}_2/\text{Au}(100\text{nm})/\text{MnO}_2$ samples, respectively. The values of energy bands tails are increased after the stacked layers of MnO_2 were sandwiched with Au layers as shown in Fig (4.7). For the energy band tails to exist, E_e must be less than half of the energy band gap. Since the lowest achievable energy band gap is larger than 3.4 eV as we will show in the following section, then all observed E_e values are related to the band tails.

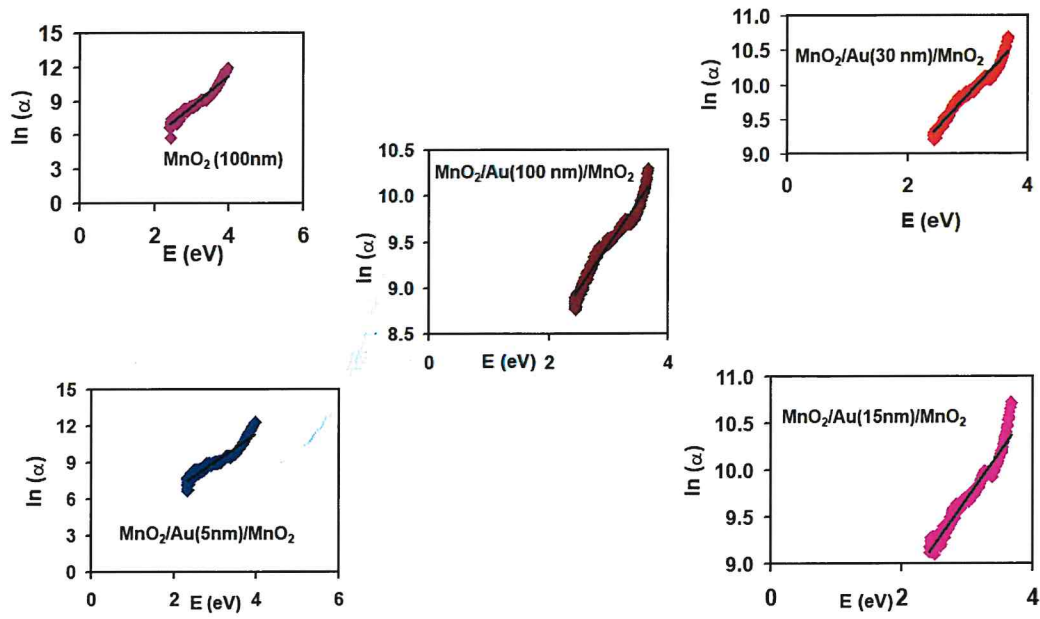


Figure 4.6: $\ln(\alpha)$ - E variation in the low absorption region for band tail investigation of the $\text{MnO}_2/\text{Au}/\text{MnO}_2$ stacked layers.

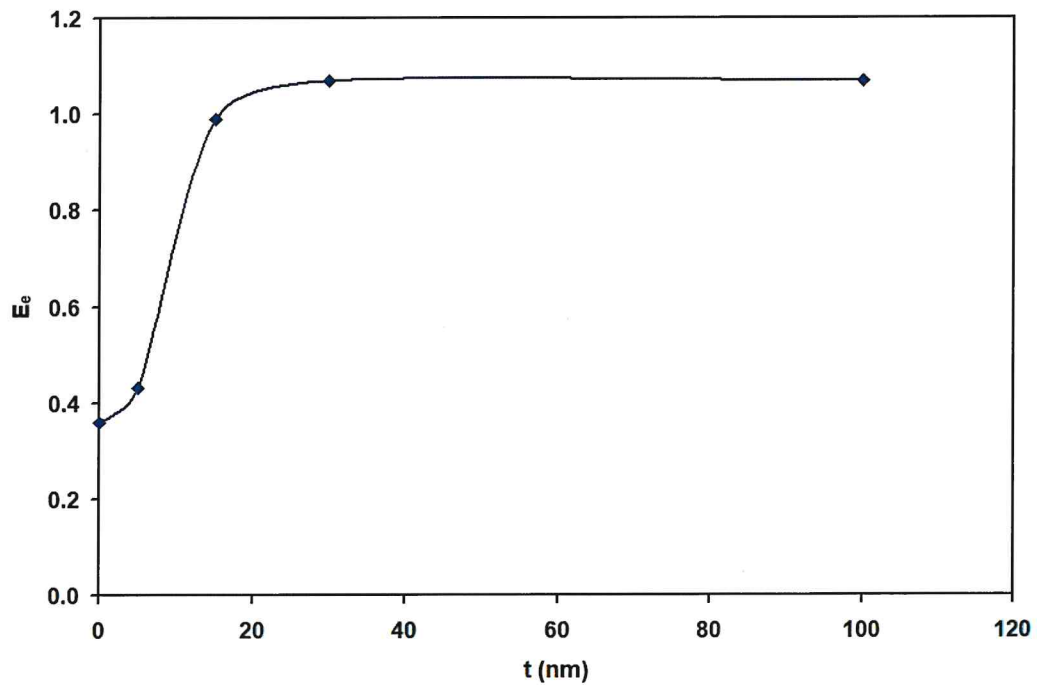


Figure (4.7): The energy bands tails of the stacked layers of MnO_2 sandwiched with Au layers as function of Au nanosheet thickness.

In the strong absorption region, the absorption coefficient spectra were analyzed in accordance with the Tauc's equation $(\alpha E)^{1/p} = B(E - E_g)$, in order to obtain more detailed information about the optical energy band gap (E_g) of the samples. The respective $(\alpha E)^2$, $(\alpha E)^{2/3}$, $(\alpha E)^{1/2}$, $(\alpha E)^{1/3}$ versus E variations were plotted and compared. As demonstrated in Fig. (4.8) The best fit of the data for all films were obtained for $(\alpha E)^{1/3} - E$ variation indicating that the band gap is of indirect forbidden transitions type. The values of E_g as calculated from the E - axis crossings are found to be 3.474 eV for unsandwiched, and 3.455, 3.435, 3.415 and 3.41 eV for the samples were sandwiched with Au layers of 0, 5, 15, 30 and 100nm, respectively. It is clear from these values that the values of energy band gaps are decreased after the stacked layers of MnO_2 sandwiched with Au layers. The $E_g - t$ (nm) variations are illustrated in Fig (4.9). The decrease in energy band gaps is due to the overlapping of atomic orbitals between Mn, O and Au atoms [42]. Particularly, as the electronic configurations of Au is $[Xe]4f^{14}5d^{10}6s^1$ [43] and that of Mn and O are $[Ar]3d^54s^2$ [44] and $1s^2 2s^2 2p^4$ [45], Au orbital states can reach higher levels in MnO_2 resulting in valance band bend up. In addition, due to the large work function of Au metal image force lowering effect is also expected. The image force bends the conduction band down resulting in E_g narrowing.

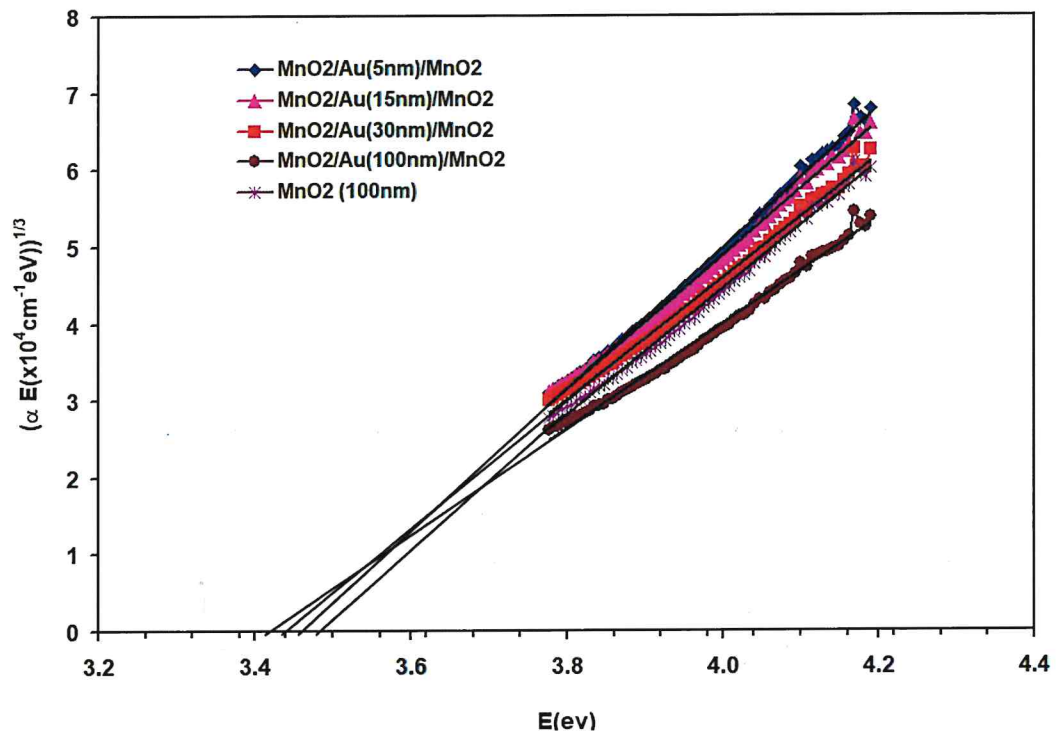


Figure 4.8: Energy band gaps investigation for the MnO₂/Au/MnO₂ stacked layers.

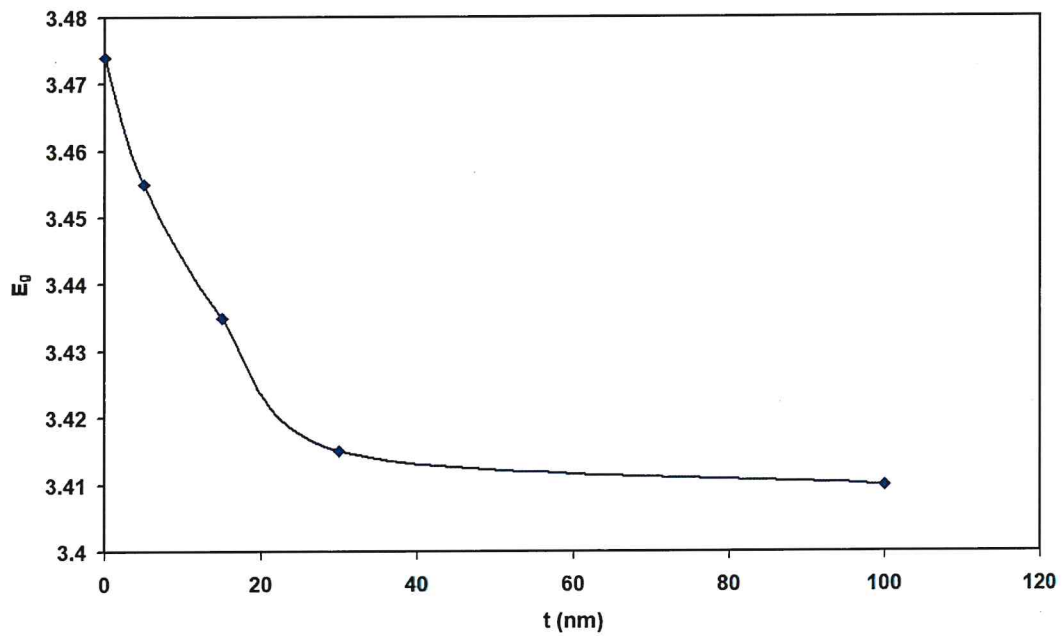
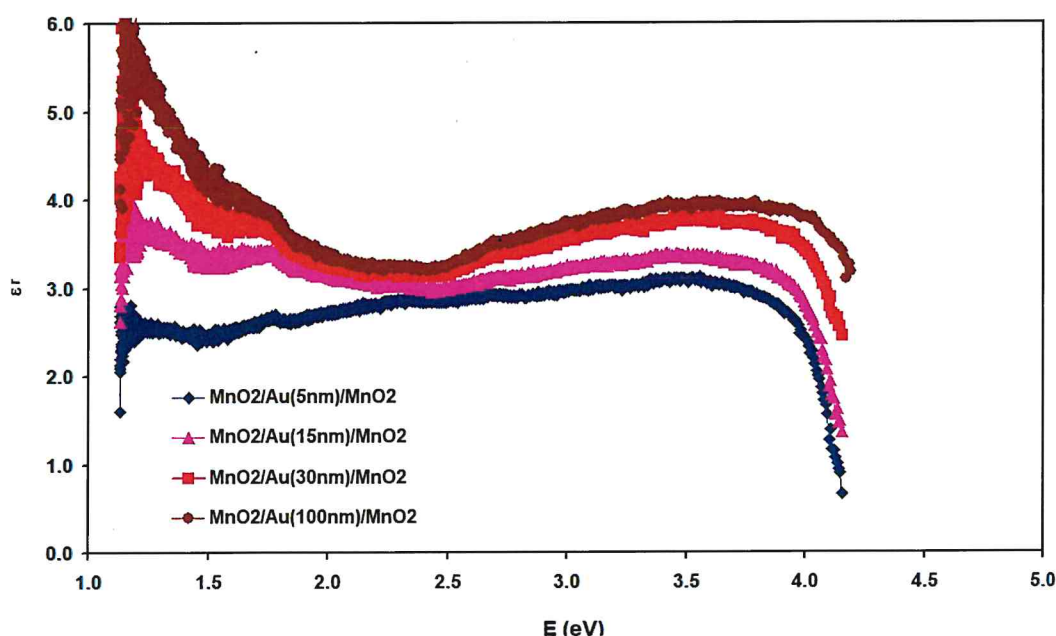


Figure 4.9: The energy band gaps of the stacked layers of MnO₂ sandwiched with Au layers as function of Au nanosheet thickness.

4.3 Dielectric dispersion

The real (ϵ_r) and imaginary dielectric (ϵ_{im}) constants are calculated from the absorption coefficient and reflectance data to obtain detailed information about the dielectric and dispersion within the films. Fig. (4.10) shows the real parts of the dielectric constant (ϵ_r) as determined from the Fresnel's equations. It can be seen that all samples exhibit the same trend of variation. The Figure shows that the samples display three significant peaks of ϵ_r spectra. For $\text{MnO}_2/\text{Au}(5\text{nm})/\text{MnO}_2$, a real dielectric constant (ϵ_r) values of 2.76, 2.69 and 2.8 corresponding to an energy values of 1.17 eV, 1.76 and 3.87 eV, respectively, are observed. The same number of peaks appeared in the other samples with an increase in the thickness of Au layers, at the same trend of variation. Also, the values of the real dielectric constant with respect to the energy value increase with increasing thickness of Au layers.



Figure(4.10): Real parts of the dielectric constant of the films measured with energy.

As shown in Fig4.11(d), in the high energy (ultraviolet range) the dielectric constant was improved. At the value of the energy of 4.0 eV, the values of the dielectric constant significantly increase until the value of thickness reached 30nm, then it tends to remain constant. In the visible range of light as shown in Fig4.11(c), at 2.5 eV of energy, the values of the dielectric constant significantly increases until the value of thickness reached 5 nm, then it remains constant. In infrared range as seen in Fig4.11(b), at 1.5 eV of energy, the values of the dielectric constant significantly

increases until the value of thickness reached 30nm, then it remains constant. The dielectric constant increases with increasing thickness of Au layers. As shown in Fig(4.10), when the energy value reaches 1.76 eV, a shoulder in the peak appears.

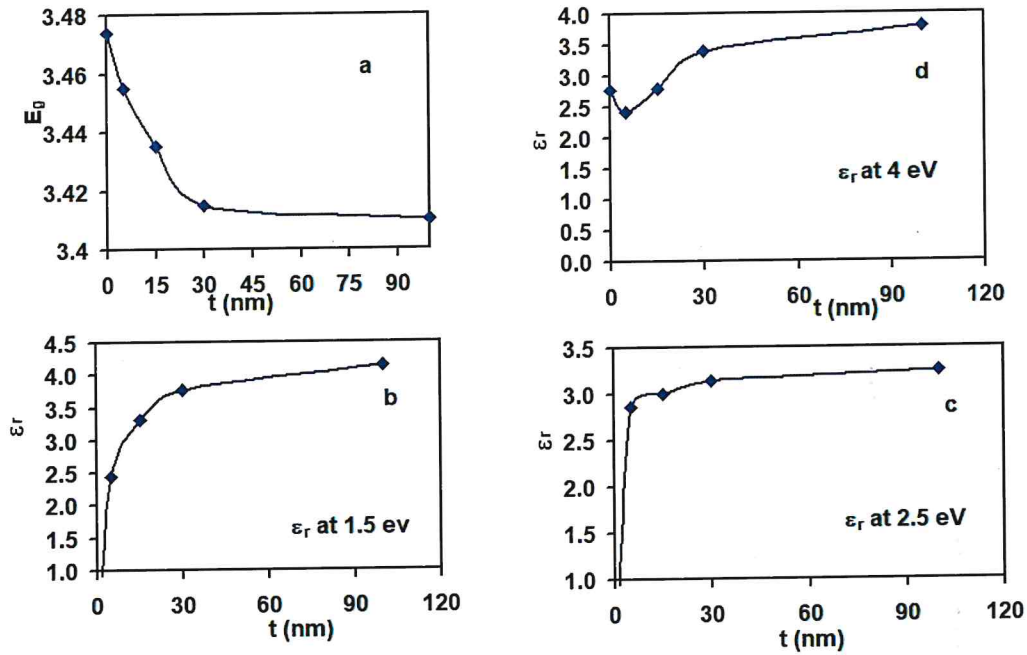


Figure 4.11. (a) the values of the energy band gaps of the films measured with thickness. (b) real parts of the dielectric constant of films measured with thickness in infrared region. (c) real parts of the dielectric constant of films measured with thickness in visible region. (d) real parts of the dielectric constant of films measured with thickness in ultraviolet region.

The imaginary part of the dielectric constant which is shown in Fig 4.12 can be used to provide information about the optical parameters. It can be seen that all samples exhibit the same trend of variation. Particularly, in the imaginary dielectric constant decreases with increasing incident photon energy until reaches 2 eV. Then it remains almost constant until reaches 3.5 eV. After that, ϵ_{im} increases with increasing incident photon energy.

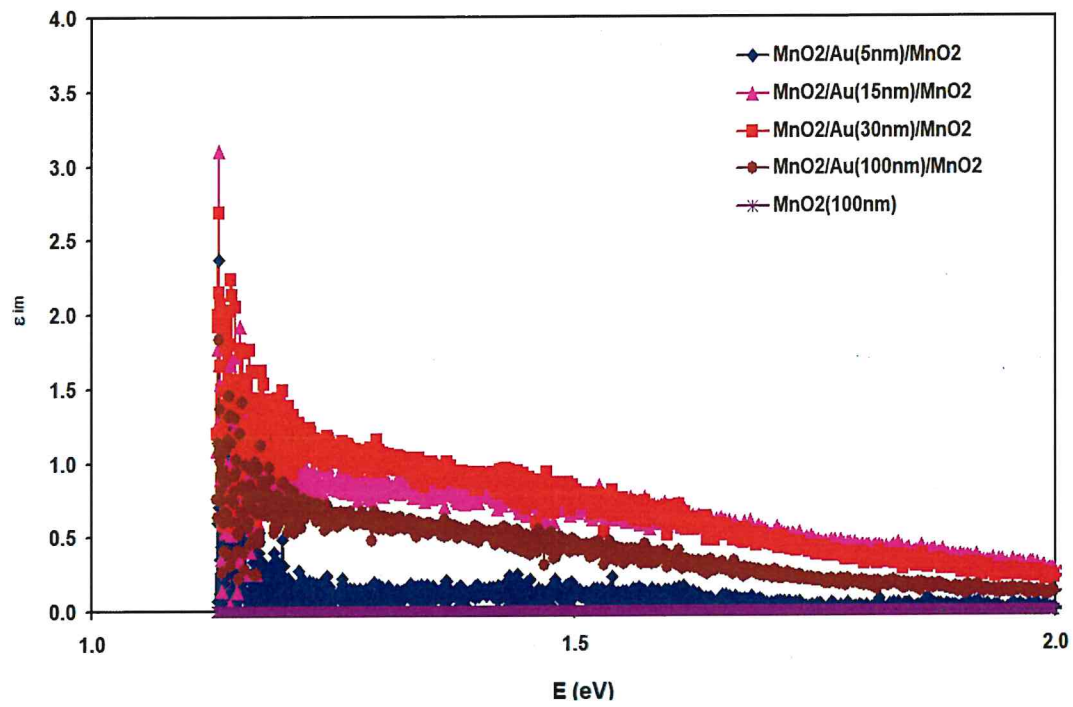


Figure 4.12: imaginary part of the dielectric constant of the $\text{MnO}_2/\text{Au}/\text{MnO}_2$ stacked layers.

Chapter 5

Conclusions

In this thesis, we have explored the effects of inserting Au nanosheets on the structural and optical properties of a thin layer on MnO_2 films. In general, MnO_2 nanosheets are of amorphous nature regardless of the Au nanosheet layer thickens. On the other hand, the optical transmittance, reflection and absorbance highly affected by Au sheets. It is observed that the energy band gap of MnO_2 comprise wide range of band tails. These tails become wider upon increasing the thickness of the Au nanosheets. In addition, accompanied with the widening of the and tails width, a shrinkage in the energy band gap is observed. Even though the energy and gap is narrowed it still in the blue-ultraviolet (UV) band range indicating the suitability of $\text{MnO}_2/\text{Au}/\text{MnO}_2$ stacked layers as UV detectors. On the other hand, insertion of Au nanosheets between layers of MnO_2 remarkable increased the real pare of the dielectric constant making the material more appropriate for high k-gate applications.

References

- [1] Dessie, Y., Tadesse, S., & Eswaramoorthy, R. (2020). Physicochemical parameter influences and their optimization on the biosynthesis of MnO₂ nanoparticles using *Vernonia amygdalina* leaf extract. *Arabian Journal of Chemistry*, 13(8), 6472-6492.
- [2] Rahman, A. U., Zarshad, N., Wu, J., Faiz, F., Raziq, F., Ali, A., ... & Ni, H. (2021). Fabrication of Ag-doped MnO₂ nanosheets@ carbon cloth for energy storage device. *Materials Science and Engineering: B*, 269, 115150.
- [3] Yang, R., Fan, Y., Ye, R., Tang, Y., Cao, X., Yin, Z., & Zeng, Z. (2021). MnO₂-Based Materials for Environmental Applications. *Advanced Materials*, 33(9), 2004862.
- [4] Makhoul MM, Preparation and optical characterization of -MnO₂ nano thin films for application in heterojunction photodiodes, *Sensors and Actuators: A. Physical* (2018).
- [5] Cao, J., Zhang, D., Zhang, X., Wang, S., Han, J., Zhao, Y., ... & Qin, J. (2020). Mechanochemical reactions of MnO₂ and graphite nanosheets as a durable zinc ion battery cathode. *Applied Surface Science*, 534, 147630.
- [6] Ma, S., Ye, X., Jiang, X., Cen, W., Jiang, W., & Wang, H. (2021). First principles calculation of mechanical, dynamical and thermodynamic properties of MnO₂ with four crystal phases. *Journal of Alloys and Compounds*, 852, 157007.
- [7] Birgisson, S., Saha, D., & Iversen, B. B. (2018). Formation mechanisms of nanocrystalline MnO₂ polymorphs under hydrothermal conditions. *Crystal Growth & Design*, 18(2), 827-838.
- [8] XIA, A., ZHAO, C., ZENG, X., HAN, Y., & TAN, G. (2021). Preparation and Electrochemical Properties of B-doped MnO₂. *Chinese Journal of Materials Research*, 35(1), 36-44.
- [9] Shah, S.I., Zulfiqar, Khan, T. et al. Study of structural, optical and dielectric properties of α -MnO₂ nanotubes (NTS). *J Mater Sci: Mater Electron* 30, 19199–19205 (2019).

- [10] Ghalkhani, M., & Sohouli, E. (2021). Effect of MnO₂ and MnO₂-NCNO addition on structural and nonlinear optical properties of CoWO₄ ceramics.
- [11] Mohammed, G. H., & Abdul Karim, H. J. (2021, November). Effect of some transitional metal oxides on the structural and optical properties of (ZnO-TiO₂) thin films. In AIP Conference Proceedings (Vol. 2372, No. 1, p. 040009). AIP Publishing LLC.
- [12] Liu, S., Li, K., Shao, D., Shen, Q., Huang, S., Ji, H., ... & Zheng, X. (2020). Dual enzyme-like activities of transition metal-doped MnO₂ nanocoatings and their dependence on the electronic band structure and ionic dissolution. *Applied Surface Science*, 534, 147649.
- [13] Khan, H., Yerramilli, A. S., D'Oliveira, A., Alford, T. L., Boffito, D. C., & Patience, G. S. (2020). Experimental methods in chemical engineering: X-ray diffraction spectroscopy—XRD. *The Canadian Journal of Chemical Engineering*, 98(6), 1255-1266.
- [14] Zhang, L., Gonçalves, A. A., & Jaroniec, M. (2020). Identification of preferentially exposed crystal facets by X-ray diffraction. *RSC Advances*, 10(10), 5585-5589.
- [15] Chatain, D., Singh, S., Courtois, B., Silvent, J., Verzeroli, E., Rohrer, G. S., ... & Wynblatt, P. (2020). Influence of step structure on preferred orientation relationships of Ag deposited on Ni (111). *Acta Materialia*, 200, 287-296.
- [16] Hirao, N., Kawaguchi, S. I., Hirose, K., Shimizu, K., Ohtani, E., & Ohishi, Y. (2020). New developments in high-pressure X-ray diffraction beamline for diamond anvil cell at SPring-8. *Matter and Radiation at Extremes*, 5(1), 018403.
- [17] Nguyen, T. D., Sierra, E., Eguiraun, H., & Lizundia, E. (2018). Iridescent cellulose nanocrystal films: the link between structural colour and Bragg's law. *European Journal of Physics*, 39(4), 045803.
- [18] Sze, S. M., & Ng, K. K. (2006). *Physics of semiconductor devices*. Hoboken, New Jersey: John Wiley & Sons. Inc.—2007.
- [19] Kittel, C. (2021). *Introduction to solid state physics* Eighth edition.
- [20] Svetikov, V., Ivonin, I., Koshelev, A., Velikov, L., Vorobiev, Y., Goltsov, A., & Yankov, V. (2011, February). Suppression of lateral modes in wide aperture laser diodes by digital planar holograms. In *High-Power Diode Laser Technology and*

Applications IX (Vol. 7918, p. 79180P). International Society for Optics and Photonics.

[21] Kulawiak, M., & Chybicki, A. (2018). Application of Web-GIS and geovisual analytics to monitoring of seabed evolution in South Baltic Sea coastal areas. *Marine Geodesy*, 41(4), 405-426.

[22] Fox, M. (1970). Optical properties of solids.

[23] Qasrawi, A. F., & Omareya, O. A. (2019). In situ observations of the permanent structural modifications, phase transformations and band gap narrowing upon heating of Cu₂Se/Yb/Cu₂Se films. *Journal of Alloys and Compounds*, 785, 1160-1165.

[24] Wager, J. F. (2017). Real-and reciprocal-space attributes of band tail states. *AIP Advances*, 7(12), 125321.

[25] Mbule, P. S. (2009). Sol-gel synthesis of and luminescent properties of Pr³⁺ in different host matrices (Doctoral dissertation, University of the Free State).

[26] Pankove, Jacques I. Optical processes in semiconductors. Courier Corporation, 2012.

[27] Hassanien, A. S., & Akl, A. A. (2016). Effect of Se addition on optical and electrical properties of chalcogenide CdSSe thin films. *Superlattices and Microstructures*, 89, 153-169.

[28] Attwood, David (1999). Soft X-rays and extreme ultraviolet radiation: principles and applications. p. 60. ISBN 978-0-521-02997-1.

[29] Aslam, M., Kalyar, M. A., & Raza, Z. A. (2017). Graphene oxides nanosheets mediation of poly (vinyl alcohol) films in tuning their structural and opto-mechanical attributes. *Journal of Materials Science: Materials in Electronics*, 28(18), 13401-13413.

[30] Karakachian, H. R. (2017). *Tuning surface phonon polaritons* (Doctoral dissertation).

[31] Sadao Adachi. The Handbook on Optical Constants of Semiconductors in Tables and Figures. Gunma University. Japan

[32] Sangian, H. F., Aruan, I., Tamuntuan, G. H., Bobanto, M. D., Sadjab, B. A., Purwadi, R., ... & Gunawan, S. (2019). A Comparative Study of the Structures,

Crystallinities, Miller Indices, Crystal Parameters, and Particle Sizes of Microwave- and Saline Water-Treated Cassava Starch. *BioResources*, 14(4), 8212-8228.

[33] Dinnebier, R. E., & Billinge, S. J. L. (2019). The Bragg equation derived.

[34] Lin, M. H., Parasuraman, P. S., & Ho, C. H. (2018). The study of near-band-edge property in oxygen-incorporated ZnS for acting as an efficient crystal photocatalyst. *ACS omega*, 3(6), 6351-6359.

[35] Chen, B., Wu, B., Yu, L., Crocker, M., & Shi, C. (2020). Investigation into the catalytic roles of various oxygen species over different crystal phases of MnO₂ for C₆H₆ and HCHO oxidation. *ACS Catalysis*, 10(11), 6176-6187

[36] Qasrawi, A. F., & Alharbi, S. R. (2020). Enhancing the optoelectronic performance of As₂Se₃ thin films via Ag slabs sandwiching. *Optik*, 219, 165228

[37] Qasrawi, A. F. (2019). EFFECT OF Y, Au AND YAu NANOSANDWICHING ON THE STRUCTURAL, OPTICAL AND DIELECTRIC PROPERTIES OF ZnSe THIN FILMS.

[38] Al Garni, S. E., & Qasrawi, A. F. (2019). Design and characterization of MoO₃/CdSe heterojunctions. *Physica E: Low-dimensional Systems and Nanostructures*, 105, 162-167.

[39] Sivakumar, T., Anbarasan, R., Sundar, J. K., & Lakshmi, M. A. (2020). Enhancing the SHG effect of zinc chloride-doped DAST single crystals: new potential materials for nonlinear optical device applications. *Journal of Materials Science: Materials in Electronics*, 31(15), 12943-12954.

[40] Dell'Olio, F., Ciminelli, C., & Armenise, M. N. (2013). Theoretical investigation of indium phosphide buried ring resonators for new angular velocity sensors. *Optical Engineering*, 52(2), 024601

[41] Skaistys, E., & Sugakov, V. I. (1971). The free-carrier absorption in polycrystals. *physica status solidi (b)*, 48(2), K99-K101

[42] Khusayfan, N. M., & Khanfar, H. K. (2018). Characterization of CdS/Sb₂Te₃ micro/nano-interfaces. *Optik*, 158, 1154-1159.

[43] Pham, M. T. J. (2018). Polar intermetallic crystals and quasicrystals (Doctoral dissertation, Iowa State University.)

[44] Abdelrahman, A., Hamouda, A., Mohamed, H., & Zaki, A. (2021). Studying and evaluating catalytic pyrolysis of polypropylene. *Egyptian Journal of Chemistry*, 64(5), 2593-2605.

- [45] Harvey, J. S. M. (1965). Hyperfine structure in ground multiplets of ^{17}O and ^{19}F . Proceedings of the Royal Society of London. Series A. Mathematical and Physical Sciences, 285(1403), 581-596.

المخلص

في هذه الرسالة ، يتم تحضير الأغشية الرقيقة من أكسيد المنغنيز بتقنية التبخير بالفراغ تحت ضغط تفريغ من 5-10 ملي بار. يتم بعد ذلك وضع الأفلام على رقائق Au النانوي في حدود 5-100 نانومتر. تمت دراسة الخصائص التركيبية والبصرية والعازلة للأغشية بواسطة تقنيات حيود الأشعة السينية وتقنيات قياس الطيف الضوئي. لوحظ أن الأغشية النانوية / Au / MnO₂ ذات طبيعة غير متبلورة بسبب احتمال وجود أكثر من مرحلة متعددة الأشكال في هيكلها. أدى إدخال رقائق النانو Au بين طبقات MnO₂ إلى تحسين الانعكاسية الضوئية وهندسة ذبول نطاق الطاقة وفجوة نطاق الطاقة وثابت العزل الكهربائي أيضًا. يتم تقديم الإنجازات من خلال تضيق فجوة النطاق وزيادة قيمة ثابت العزل. ويلاحظ أيضًا أن التوزيع الأسّي لذيول نطاق الطاقة أصبح أوسع نتيجة تداخل حالات المدار Au / MnO₂. في ضوء الخصائص المذكورة أعلاه ، يمكن ترشيح MnO₂ nanosheets للتطبيقات الإلكترونية الضوئية.